

REPORT DOCUMENTATION PAGE				Form Approved OMB No. 0704-0188	
Public reporting burden for this collection of information is estimated to average 1 hour per response, including the time for reviewing instructions, searching existing data sources, gathering and maintaining the data needed, and completing and reviewing this collection of information. Send comments regarding this burden estimate or any other aspect of this collection of information, including suggestions for reducing this burden to Department of Defense, Washington Headquarters Services, Directorate for Information Operations and Reports (0704-0188), 1215 Jefferson Davis Highway, Suite 1204, Arlington, VA 22202-4302. Respondents should be aware that notwithstanding any other provision of law, no person shall be subject to any penalty for failing to comply with a collection of information if it does not display a currently valid OMB control number. PLEASE DO NOT RETURN YOUR FORM TO THE ABOVE ADDRESS.					
1. REPORT DATE (DD-MM-YYYY) 09/28/2012		2. REPORT TYPE Final Performance Report		3. DATES COVERED (From - To) 7/01/2007-6/30/2012	
4. TITLE AND SUBTITLE (MURI-07) Bioinspired Supramolecular Enzymatic Systems				5a. CONTRACT NUMBER	
				5b. GRANT NUMBER FA9550-07-1-0534	
				5c. PROGRAM ELEMENT NUMBER	
6. AUTHOR(S) Chad Mirkin, Mark Ratner, Joe Hupp, SonBinh Nguyen, J. Fraser Stoddart				5d. PROJECT NUMBER	
				5e. TASK NUMBER	
				5f. WORK UNIT NUMBER	
7. PERFORMING ORGANIZATION NAME(S) AND ADDRESS(ES) Northwestern University Department of Chemistry 2190 Campus Drive/Ryan Hall Evanston, IL 60208				8. PERFORMING ORGANIZATION REPORT NUMBER	
9. SPONSORING / MONITORING AGENCY NAME(S) AND ADDRESS(ES) Dr. Hugh De Long Air Force Office of Scientific Research 875 N Randolph St, Room 3112 Arlington, VA 22203				10. SPONSOR/MONITOR'S ACRONYM(S) AFOSR	
				11. SPONSOR/MONITOR'S REPORT NUMBER(S)	
12. DISTRIBUTION / AVAILABILITY STATEMENT Approved for public release; distribution unlimited.					
13. SUPPLEMENTARY NOTES n/a					
14. ABSTRACT Through the use of enzymes and related structures, Nature takes a complex, integrated approach to regulating cellular activities such as signal cascades, molecular transport, and catalysis. These critical functions are performed using information storage and retrieval processes that make use of molecular recognition. The ability to learn from Nature and mimic its processes for abiotic purposes holds great potential for controlling chemical processes and creating a wide variety of functional materials and devices that can impact military and civilian needs. Materials and devices of interest include chemical and biological detection systems, catalytic systems for environmental remediation, and materials for power applications. They will significantly impact efforts to monitor and deter the use of biological and chemical weapons, as well as hazardous explosive devices. They also will lead to more efficient, portable, and inexpensive ways of operating energy-consuming devices important to the military. Our MURI efforts aim to understand and develop a supramolecular toolbox that enables researchers to create abiotic enzymatic systems. Synthetic organic and inorganic chemistries are employed in parallel with macromolecular modeling in order to create molecular machines based on mechanostereochemical bonds, porous hybrid materials, and stimuli-responsive metal-organic supramolecular structures. These structures exhibit a full range of bio-inspired functions.					
15. SUBJECT TERMS n/a					
16. SECURITY CLASSIFICATION OF:			17. LIMITATION OF ABSTRACT Unlimited	18. NUMBER OF PAGES	19a. NAME OF RESPONSIBLE PERSON Chad A. Mirkin
a. REPORT Unclassified	b. ABSTRACT Unclassified	c. THIS PAGE Unclassified			19b. TELEPHONE NUMBER (include area code) 847-491-2907

Final Performance Report

MURI: Bioinspired Supramolecular Enzymatic Systems

Grant Number: FA9550-07-1-0534

Principal Investigator: Chad A. Mirkin

Program Manager: Hugh De Long

1. SUMMARY

We have used supramolecular chemistry to construct new artificial enzymes and enzyme-mimics that address DoD-relevant scientific and technological challenges in three broad areas: (a) chemical *transformation*, (b) chem/bio *protection*, and (c) chem/bio *detection*. In each area, we began with comparatively simple challenges and/or supramolecular systems and then escalated toward the most sophisticated systems and most difficult problems. Specifically, we demonstrated: (a) mesoscale fabrication and (b) entatic behavior in artificial systems. We have built systems that functionally mimic transferases, decarboxylases, oxygenases and other classes of enzymes. With these capabilities in place, we then sought: (a) to build supramolecular systems which acted as true biological mimics in the context of catalytic reactions that require O₂ and C-H bond activation and functionalization, and (b) to design allosteric catalysts that are reminiscent of ELISA (Enzyme-Linked ImmunoSorbent Assay) and PCR (Polymerase Chain Reaction) where small amounts of analyte can be detected through initiating a binding event which in turn serves to increase and amplify signal or product production. The multidisciplinary work accomplished integrated efforts and expertise in organic and inorganic chemical synthesis, assembly, and materials characterization. Computational modeling (molecular dynamics simulations, electronic structure calculations) was used for mechanism prediction and assessment, engineering of optimal analyte/substrate recognition and binding, and measurement of abiotic catalytic activity for analyte detection. Main focuses of the grant period were on low-value substrate to high-value product conversion, pollutant destruction, and agent destruction.

2. ACCOMPLISHMENTS/FINDINGS

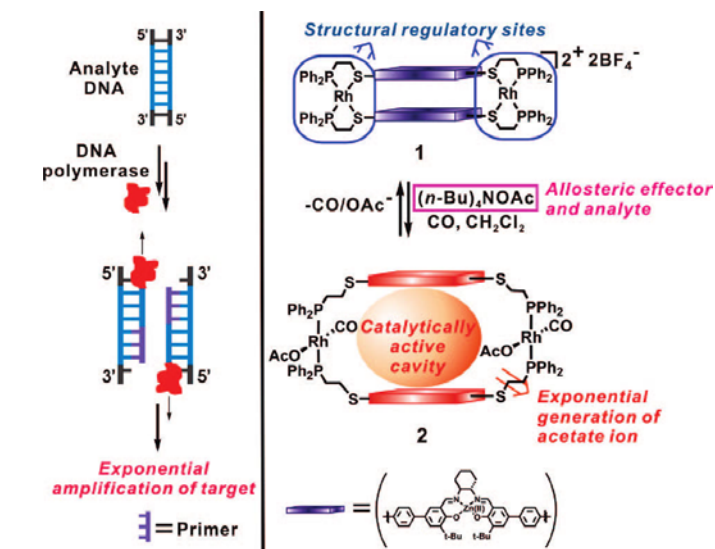
2.1 PCR-Like Cascade Reactions in the Context of an Allosteric Enzyme Mimic

Over the course of the MURI grant period, **Mirkin, Hupp, Stoddart, Ratner, and Nguyen** made significant headway into the synthesis and study of supramolecular allosteric enzyme mimics. Since biological systems are capable of highly specific chemical transformations and detection, but biological building blocks are generally considered chemically fragile, the construction of abiotic enzyme mimics that can perform such transformations and detections is highly relevant to DoD scientific and technological goals. The nanoscale environment created by a supramolecular complex is desirable for such tasks, as it can be significantly different from its exterior environment and used to increase the speed of a chemical reaction, alter reaction routes, control stereochemistry, affect oligomerization processes, or extend the lifetimes of highly reactive molecules.

One of the major achievements during the grant period was the development of the first abiotic allosteric catalyst reminiscent of PCR by the **Mirkin** group. PCR is extensively used in the biological community for amplifying DNA through copying the

sequence of a specific nucleic acid target. When coupled with diagnostic probes, this technique allows one to detect a small collection of molecules under very dilute conditions.

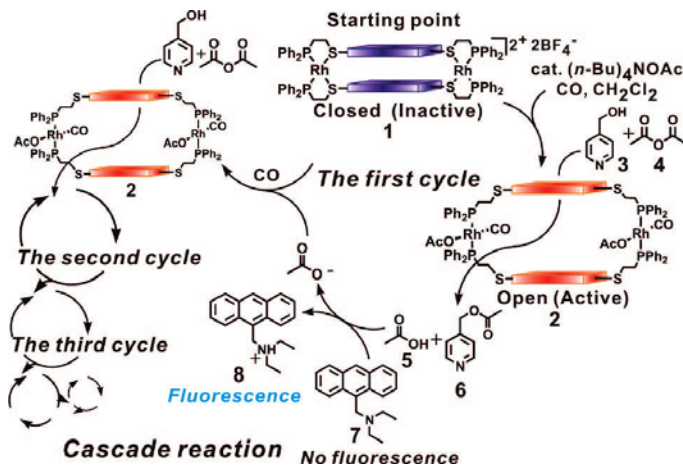
PCR-based methods are the backbone of the modern biodiagnostics industry and allow one to identify genetic markers with unprecedented sensitivity and very high reliability. However, PCR only works with nucleic acid targets, and there are no known analogs of this technique for other target molecule candidates. If one could find a way to amplify non-nucleic acid



Scheme 1. Small-molecule regulated target amplification with an allosteric enzyme mimic.

targets, it should be possible to create ultrasensitive detection systems for a much wider class of analytes, including those that are important for biological and non-biological applications.

Consequently, the **Mirkin** group designed a coordination chemistry-based system that mimics the properties of PCR. Specifically, this allosteric enzyme mimic recognizes a small molecule through metal ligand binding at a regulatory site, subsequently turning on a catalytic reaction that generates more of the same molecule that was initially recognized. This is the first example of a coordination chemistry-based catalytic system that mimics some of the properties of PCR in the context of a small molecule, rather than a nucleic acid, recognition event and exhibits the cascade amplification curves typically associated with a PCR-like reaction. Specifically, the WLA-assembled tetranuclear complex **1** (Scheme 1) was opened in the presence of Cl^- to generate a cavity capable of catalyzing an acyl transfer reaction between



Scheme 2. Proposed cascade mechanism for the PCR-mimic in the context of acetate detection.

pyridyl carbinol and acetic anhydride. When carried out under basic conditions, acetate is produced as a byproduct of this reaction. In order to evaluate the suitability of acetate to act as an allosteric effector, complex **1** was reacted with two equivalents of (*n*-Bu)₄NOAc at room temperature under a CO atmosphere. Significantly, it quantitatively converted to the open macrocycle **2**, which possesses a *trans* acetate and CO ligand at each Rh(I) site.

The open macrocycle **2** was characterized by ¹H and ³¹P{¹H} NMR spectroscopy, FT-IR spectroscopy and electrospray ionization mass spectrometry (ESI-MS). All data were consistent with the proposed structural formulation, and the reaction was completely reversible. Indeed, upon removal of solvent and CO by vacuum, complex **1** quantitatively reformed. These experiments confirmed that the acetate anion can act as an allosteric effector to chemically toggle the macrocycle from a closed and inactive to an open and catalytically active state.

The catalytic activity of the Zn(II)-salen based supramolecular compounds **1** and **2** was studied in the context of the acyl transfer reaction involving acetic anhydride and pyridyl carbinol as the substrates (**Scheme 2**). In the absence of acetate, there is almost no catalytic activity. However, if 1 mL of 0.04 mM (433 nmol) (*n*-Bu)₄NOAc is added to a 10 mL solution containing 4.44 μmol (0.4 mM) of inactive macrocyclic complex **1**, CO (1 atm), 13.5 μmol of the substrates (pyridyl carbinol **3** and acetic anhydride **4**, 1.22 mM), and 13.5 μmol of the fluorophore (9-(*N,N*-diethylaminomethyl)anthracene **7**, 1.22 mM), the mixture begins to catalyze the acyl transfer reaction. Once a small amount of (*n*-Bu)₄NOAc reacts with inactive complex **1** at its two rhodium centers that serve as structural regulatory sites, the complex is converted into open cavity complex **2**, which then catalyzes the reaction between **3** and **4** (**Scheme 2**). In the early stages of the reaction, only a minor amount of the catalyst is activated (in the form of **2**, ~5% based upon stoichiometry), but as the reaction proceeds, more acetate is generated, leading to the formation of more **2** and progressively faster catalysis. The pH-sensitive fluorescent dye **7** allows one to follow the amount of acetate generated during the catalytic cycles. This type of cascade reaction results in an exponential increase of the amount of products **5** and **6**.

The formation kinetics of the product, 4-acetoxymethylpyridine, **6** were studied by gas chromatography (GC) as a function of starting acetate concentration (**Figure 1**). Significantly, one sees the sigmoidal product generation curves, which are characteristic of PCR-like processes and reminiscent of those observed in the study of autocatalytic and self-replicating systems with synthetic macromolecules, such as cylindrical dimeric capsules and adenine-imide conjugate molecules. Slow induction, followed by rapid exponential amplification, linear growth and then eventual saturation (after ~80% of the

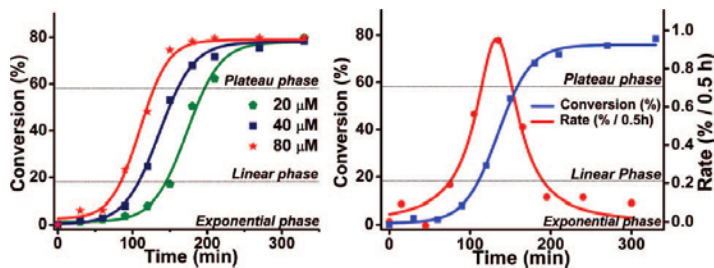


Figure 1. Conversion (%) vs. time (min) starting with various concentrations of analyte (left). Conversion (■) and rate (●) vs. time in the case of 40 μM of analyte (right). Product formation was monitored by GC (product **6**) and fluorescence (acetate ion by pH indicator).

substrate has been consumed) stages are observed, regardless of initial analyte concentration. As with PCR, the time at which the exponential step turns on correlates with the analyte concentration.

In conclusion, **Mirkin** presented the first demonstration of a PCR-type cascade reaction involving a supramolecular allosteric catalyst where a catalyst is activated by recognition of a small molecule, which leads to the catalytic generation of more analyte, generating a cascade that resembles the amplification processes in PCR.

2.2 Allosteric Regulation of a Supramolecular Triple-Layer Catalyst

Another highlight of the grant period involved the development of a new supramolecular architecture by **Mirkin** and **Nguyen**. For the past several decades, researchers have evaluated supramolecular coordination complexes in the context of

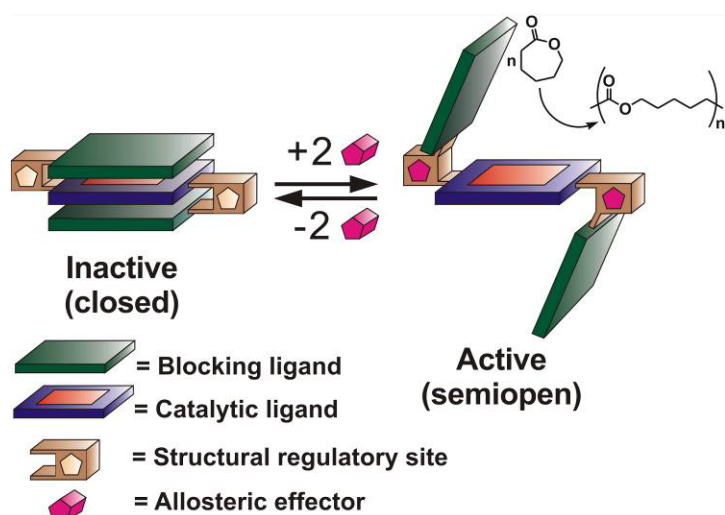


Figure 2. A model of an allosteric supramolecular triple-layer complex for the regulation of the catalytic living polymerization of ϵ -caprolactone.

can be significantly different from its exterior environment and used to increase the speed of a chemical reaction, alter reaction routes, control stereochemistry, affect oligomerization processes, or extend the lifetimes of highly reactive molecules such as cyclobutadiene. There are three general methods for synthesizing supramolecular coordination complexes, termed the directional bonding (DBA), symmetry interaction (SIA), and weak-link (WLA) approaches. The DBA and SIA yield structurally rigid complexes while the WLA produces rigid intermediates, which can be chemically interconverted with structurally flexible cage-like products. **Mirkin** and **Nguyen** utilized such interconversions to synthesize and study a new class of multimetallic allosteric complexes for molecular recognition and catalytic purposes.

catalysis, sensing, molecular electronics, mixture separations, recognition of small-molecules, and facilitated small-molecule transport. Such systems are interesting because they often mimic the properties of biological systems and can be used to generate novel agents with well-defined cages and corresponding encapsulating properties. The nanoscale environment created by a supramolecular complex

All allosteric supramolecular systems developed thus far rely on the use of homoligated macrocycles or tweezers with pockets based upon catalysts that function in a bimetallic fashion. However, if one could expand the repertoire of allosteric systems from bimetallic to monometallic structures, myriad possibilities in the area of allosteric catalysis would result. Ideally, one would like access to a structure with a single catalytic

site that is blocked above and below by chemically inert entities, which can be opened and closed through chemical stimuli at remote regulatory sites (Figure 2).

The **Mirkin** and **Nguyen** groups pioneered the synthesis of a triple-layer complex (TLC), which is composed of two transition metal nodes, two chemically inert blocking exterior layers, and a single catalytically active interior Al(III)-salen complex, which can act as a ring-opening polymerization catalyst

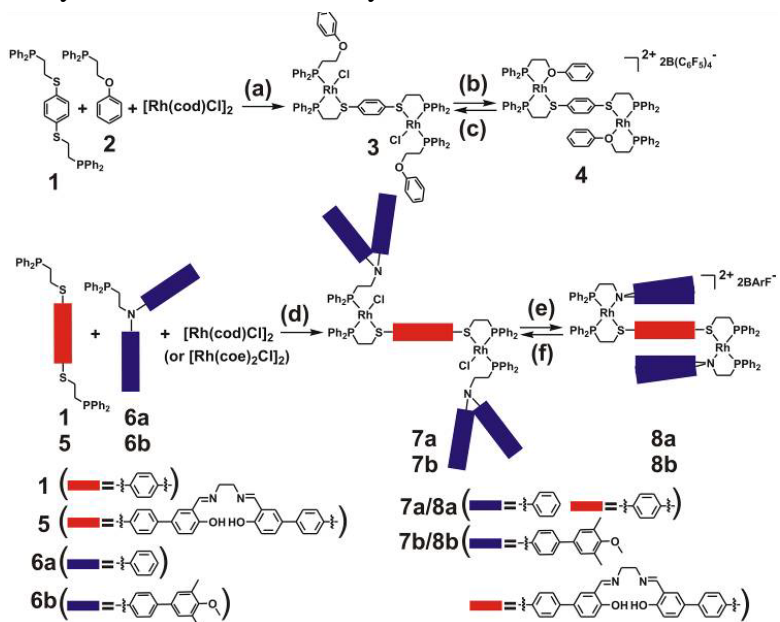


Figure 3. Synthetic scheme depicting means of constructing a model triple-layer allosteric polymerization catalyst.

with ϵ -caprolactone (ϵ -CL) as the substrate. This complex was synthesized through the WLA and a halide-induced ligand rearrangement process (HILR) and can be reversibly activated and deactivated through small-molecule reactions that assemble and disassemble the trilayer structures, allowing one to reversibly activate the catalytic site by exposing and subsequently blocking it.

In an effort to design a catalytic system in the form of a triple-layer structure, **Mirkin** and **Nguyen** initially studied the coordination chemistry of previously synthesized complex **3** (Figure 3). This complex can be reversibly interconverted with the triple-layer structure **4**, by the abstraction and subsequent addition of Cl^- ligand. To realize the targeted triple-layer catalyst structure, **Mirkin** and **Nguyen** had to design a system that did not involve a Rh-O linkage as in compound **4**; this linkage is too easily broken by relatively weakly binding ligands, and therefore presents a functional group incompatibility issue with many catalytic reactions. In order to synthesize a more robust structure, **Mirkin** and **Nguyen** first replaced the ether moiety with an amine which forms a stronger coordination bond with Rh(I) than the ether. Amine-containing neutral semi-open complex **7a** was synthesized in 97% yield by reacting one equiv of $[\text{Rh}(\text{cod})\text{Cl}]_2$ (cod = 1,5-cyclooctadiene) with two equiv of PN ligand **6a** and one equiv of PS bidentate ligand **1** in dry CH_2Cl_2 at room temperature. All analytical data, including ^1H NMR spectroscopy, $^{31}\text{P}\{^1\text{H}\}$ NMR spectroscopy, and ESI-MS (Electrospray Ionization Mass Spectrometry) are in full agreement with the proposed structural formulation.

The catalytic properties of closed compound and semi-open metallated (Al^{3+}) salen-based systems were tested in terms of a ring opening polymerization of ϵ -CL. This system is outstanding for evaluating the potential for allosteric control in the context of a living catalyst. Indeed, many researchers would like the ability to regulate the activity of catalysts so that one could control catalytic reaction rates and product distributions, in situ, and as in this proof-of-concept case, polymer growth and molecular weight. In a typical experiment, semi-open catalyst (2.09 mM) was added to a toluene- d_8 solution of ϵ -CL (331 or 541 mM), and the formation of the product, polycaprolactone (PCL), was monitored by ^1H NMR spectroscopy as a function of time. **Mirkin** and **Nguyen** made

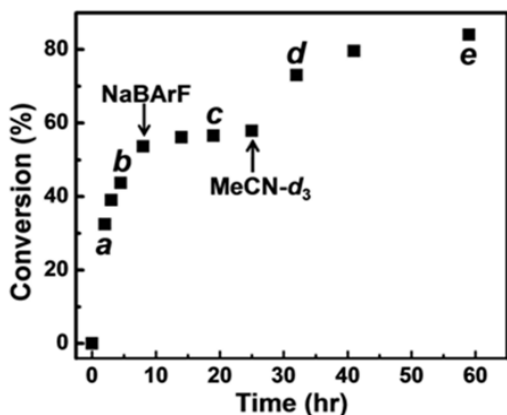


Figure 4. Allosteric regulation of lactone polymerization catalyst, as observed from polymer conversion profile.

demonstrated that one could allosterically regulate the catalytic activity of the supramolecular catalyst with small-molecules (**Figure 4**). As a proof-of-concept experiment, the catalyst was deactivated by adding a stoichiometric amount of the Cl^- ligand abstracting agent, NaBArF, which resulted in the clean formation of the fully closed complex, as evidenced by $^{31}\text{P}\{^1\text{H}\}$ NMR spectroscopy. Addition of acetonitrile to the closed catalyst yields the semi-open structure again, and reactivates the catalyst, allowing ϵ -CL to react with the Al(III) -salen moiety resulting in polymer growth. A linear relationship between percent of substrate conversion to product and M_n of the polymer was observed, which confirms that the catalyst maintains its catalytic activity during the allosteric regulation process. Indeed, reactivation of the catalyst results in increased M_w , due to the living nature of the polymerization and not just the generation of additional polymer of a M_w comparable to the first stage of activation.

The allosteric triple-layer catalyst reported by **Mirkin** and **Nguyen** is a first step towards man-made chemical systems that should allow one to regulate a wide variety of chemical reactions with activities, regioselectivities, and perhaps stereoselectivities that can be controlled with small molecule and elemental anion effectors. Indeed, the ability to introduce a variety of functional groups into an A–B–A type of triple-layered structure *via* coordination chemistry and the WLA is a powerful and potentially very general way of creating sterically protected catalytically active centers that can be completely

several interesting observations from this study. The first observation is that, while the semi-open compound was active and capable of quantitatively polymerizing all of the ϵ -CL monomer, the closed compound is almost completely inactive under identical conditions. The polymers produced by the reactions were characterized by ^1H , $^{13}\text{C}\{^1\text{H}\}$ NMR spectroscopy, gel permeation chromatography (GPC), and differential scanning calorimetry (DSC) in order to confirm the molecular structure of the polymer and to determine their number average molecular weights (M_n), weight average molecular weights (M_w), and polydispersity indices (PDI). More interestingly, **Mirkin** and **Nguyen**

activated and deactivated *in situ* without significant loss of catalytic activity and therefore should find utility in many areas of polymer chemistry and small molecule catalysis.

2.3 Towards Supramolecular Systems From Purely Abiotic Building Blocks

Ligand design can be used to influence the chemical properties of small molecules, catalysts, supramolecular assemblies, surfaces, and nanomaterials. Typically, the properties of ligands are adjusted by the covalent attachment of electron-donating or -

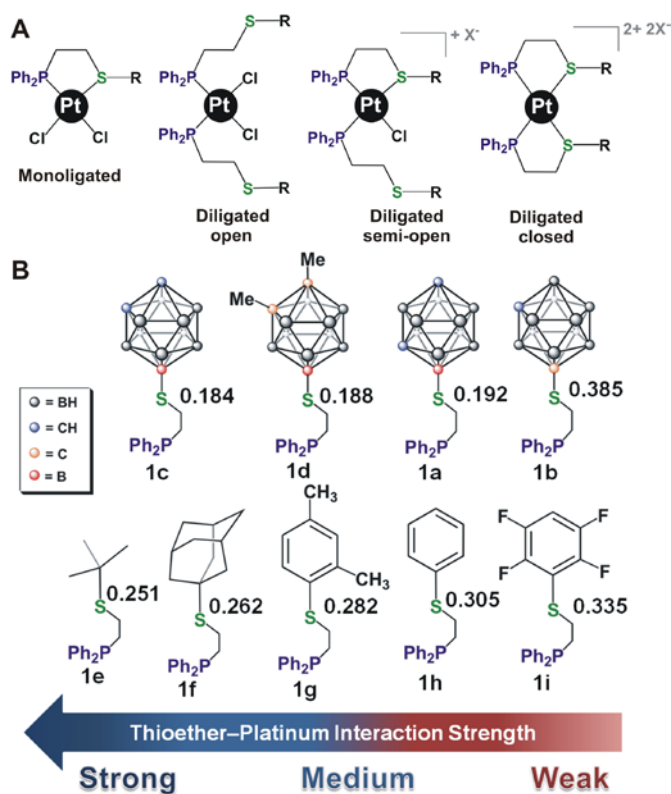


Figure 5. (A) Coordination-based motifs derived from various possible interactions of hemilabile P,S ligands with Pt(II), and (B) comparison between carbon-based and carborane-based ligands and corresponding Mulliken charge densities on S atoms associated with the thioether moieties of the ligands.

a moiety with the ability to adjust electron-donating or -withdrawing properties without significantly affecting the steric properties of the substituent.

Icosahedral carboranes are an interesting class of exceptionally stable boron-rich clusters that can be easily modified at different vertices via straightforward chemical reactions. While the coordination chemistry of carboranes has been extensively studied over the past several decades, no group has systematically studied how direct positional attachment of heteroatoms to carboranes affects the electronics of such substituents in the context of their corresponding metal-coordinating abilities. This difference can be attributed to the 3D aromatic character of the C₂B₁₀H₁₂ carborane cluster and the fact that the more electronegative C atoms contribute more electrons to cluster bonding than

withdrawing groups to the heteroatom involved in metal bonding or through the use of groups that can influence reactivity based upon relative degrees of steric bulk. The majority of such property-adjusting groups have been carbon based, with a few notable exceptions in the area of silicon chemistry. As a general rule, alkyl-based moieties are electron-donating, while aryl-based ligands are considered more electron-withdrawing. Often, aryl and alkyl moieties are used to change the steric constraints or electronic properties of a ligand, but it is difficult to do so without simultaneously affecting both the sterics and electronics of a given ligand. This is especially true if dramatic changes in electronics are required (for example in converting a ligand from very electron-donating to the other extreme). Ideally, one would like

the B atoms, which results in the C atoms effectively being electron deficient (hence their electron-withdrawing character). These features are experimentally observed from dipole measurements, where in ortho-carborane, for example, there is a net dipole moment of 4.45 that points away from two carbon vertices. **Mirkin, Ratner, and Hupp** discovered that icosahedral carboranes can be used as substituents in phosphino-thioether hemilabile ligands where the point of attachment of the sulfur to the carborane dictates the electronic properties of the thioether without significantly affecting the steric properties of the ligand.

Mirkin and Hupp have been exploring the metal-binding properties of polydentate hemilabile ligands for the past two decades. Specifically, **Mirkin** has shown how large supramolecular constructs, which mimic the properties of allosteric enzymes,

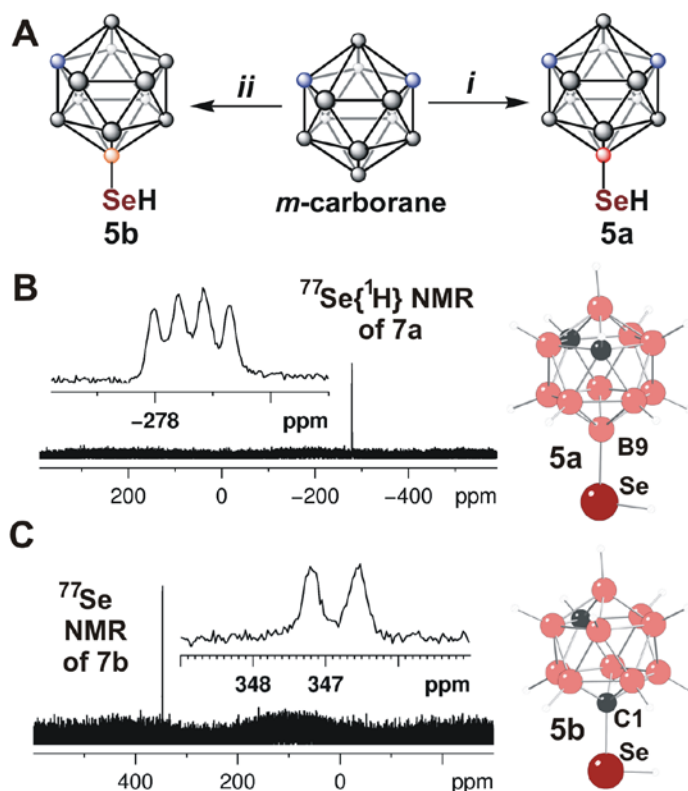


Figure 6. (A) Synthetic scheme, conditions: (i) Se_2Cl_2 , CH_2Cl_2 , AlCl_3 , aqueous workup followed by reduction w/ NaBH_4 in EtOH; (ii) $n\text{-BuLi}$, diethyl ether, 0°C to RT, then elemental Se; (B)-(C) Representative $^{77}\text{Se}/^{77}\text{Se}\{^1\text{H}\}$ NMR spectra of *m*-carborane selenol derivatives 5a and 5b and their computational models, respectively.

can be assembled via the WLA. By virtue of the hemilabile ligands used to construct WLA complexes, small molecules can be used to chemically toggle them between flexible open and rigid closed architectures. This is achieved by a reversible cleavage of weak M–X bonds, while the stronger M–P bonds remain unchanged. Therefore, it is crucial to be able to control the electronic nature of the metal-binding heteroatoms, and often one would like to do so without affecting steric considerations. In the context of a hemilabile ligand, the coordination strength of a carborane-functionalized thioether to Pt(II) can be significantly altered via the positional attachment of the heteroatom (specifically, sulfur) at different vertices of the boron-rich cluster (**Figure 5**). Strikingly, the $^{77}\text{Se}\{^1\text{H}\}$ NMR spectrum of the C-functionalized *m*-carborane selenol 5b (**Figure 6**) exhibits a resonance very far downfield at δ 347 in CD_2Cl_2 . As a point of reference, the ^{77}Se NMR spectrum of CF_3SeH , perhaps the most electron-withdrawing carbon-based selenol derivative, exhibits a resonance at δ 287.48. In contrast, the B(9)-functionalized *m*-carborane selenol 5a exhibits an extremely upfield resonance at δ –280, which appears as a quartet due to coupling to the adjacent ^{11}B nuclei ($S=3/2$). This resonance indicates that

can be assembled via the WLA. By virtue of the hemilabile ligands used to construct WLA complexes, small molecules can be used to chemically toggle them between flexible open and rigid closed architectures. This is achieved by a reversible cleavage of weak M–X bonds, while the stronger M–P bonds remain unchanged. Therefore, it is crucial to be able to control the electronic nature of the metal-binding heteroatoms, and often one would like to do so without affecting steric considerations. In the context of a hemilabile ligand, the coordination strength of a carborane-functionalized thioether to Pt(II) can be significantly altered via the positional attachment of the heteroatom (specifically,

the electron-donating B(9)-functionalized *m*-carborane cage is far more shielding than any known alkyl-based substituent. Indeed, theoretical calculations of Mulliken charges (0.038 for Se in **5a** and 0.270 in **5b**) and ^{77}Se NMR shielding constants support these experimental observations. While a ~ 625 ppm shift difference is virtually unattainable with the same carbon-based substituent, one single carborane-based moiety (*m*-carborane) can successfully serve as both an extremely electron-withdrawing or extremely electron-donating moiety.

Mirkin and **Hupp's** work suggests that a thioether moiety attached to different vertices of icosahedral carboranes can experience either a strongly electron-withdrawing (similar to fluorinated aryls), or strongly electron-donating (similar to electron-donating bulky alkyls) influence. This dichotomy is an intrinsic property of the carborane moiety, and thus one can envision that many heteroatoms attached to the sulfur atom in a similar fashion can be tuned in such a manner. This conclusion is supported by the unprecedented difference in the ^{77}Se NMR chemical shifts obtained for B(9) and C(1)-functionalized meta-carborane selenols. This also suggests that referring to a carborane (or carboranyl) moiety solely as electron-withdrawing, without specifying its point of attachment, is not rigorously correct. Overall, given that icosahedral carboranes are extremely robust and relatively inexpensive, these and many other features associated with using them as building blocks to modulate heteroatom-metal interactions can complement existing approaches in ligand design via conventional carbon-based substituents.

2.4 Pseudo-Allosteric Regulation of the Anion Binding Affinity of a Macrocyclic Coordination Complex

Biological systems that employ ion channels often use allosteric regulatory sites to control the recognition and transport of ions across membranes. However, the extension of this concept to man-made coordination-based systems is limited. This prompted us to consider how one might design a coordination complex with anion binding properties that can be allosterically controlled (**1-4**, **Figure 7**). **Mirkin** synthesized and characterized one such complex based upon a Rh^{I} macrocycle **1** synthesized via the WLA.

The synthesis of the model macrocycle **1** was achieved through synthesis of new PS hemilabile ligands, which upon complexation with Rh^{I} , led to the formation of a cyclic dinuclear Rh^{I} complex **1** in high yield. Complex **1** exhibits a single $^{31}\text{P}\{^1\text{H}\}$ NMR resonance at δ 65.1 (d, $J_{\text{Rh-P}} = 162$ Hz), which is highly diagnostic of κ^2 -P,S ligand coordination to Rh^{I} . The ^1H NMR spectrum shows a single resonance for the amide proton at δ 9.50 and aromatic resonances similar to those of the metal-free ligand, indicating a symmetric structure in solution. Electrospray ionization mass spectrometry (ESI-MS) of **1** exhibited a parent ion at 908 m/z corresponding to the $[\text{M} - 2\text{B}(\text{C}_6\text{F}_5)_4]^{2+}$ ion. Elemental analysis of the complex also supported the proposed structure. The solid-state structure of **2** was confirmed by a single-crystal X-ray diffraction study. The Rh^{I} centers exhibited distorted-square-planar geometries with *cis*-S and *cis*-P coordination environments. Four N-H protons were directed towards the center of the macrocycle, suitable for anion binding.

The condensed macrocycle **1** can be opened quantitatively into a structurally flexible macrocycle **2** by reacting it with $t\text{BuNC}$ in CH_2Cl_2 (**Figure 7**). Complex **2** exhibits a single $^{31}\text{P}\{^1\text{H}\}$ NMR resonance at δ 18.2, indicating $\kappa^1\text{-P,S}$ coordination. Complexes with two or three isocyanides on each Rh^{I} center are possible products, but based upon ^1H NMR spectroscopic studies and integration of resonances associated with the $t\text{Bu}$ groups, the tris-isocyanide structure can be ruled out. The conclusion that there are two rather than three isocyanides per Rh^{I} center is also supported by elemental analysis. The trans configuration of **2** can be confirmed based upon a comparison with known simpler model complexes.

Most interestingly, the Cl^- association constants (K_a) of **1** and **2**, measured in CH_2Cl_2 at 23 °C are significantly different. The open macrocycle **2** has a K_a ($2.5 \times 10^6 \text{ M}^{-1}$) approximately two orders of magnitude larger than the condensed macrocycle **1** ($4.2 \times 10^4 \text{ M}^{-1}$) because of the conformational flexibility of **2** as compared to **1**, which allows it to adopt a more optimal geometry for Cl^- binding.

In summary, **Mirkin** synthesized a macrocyclic complex **1** that can react with small molecules to induce a ring expansion, which significantly increases its affinity for the chloride ion (60-fold increase). The expansion leads to greater conformational flexibility of the amide groups responsible for Cl^- binding, as shown by solid-state structures and solution spectroscopic data.

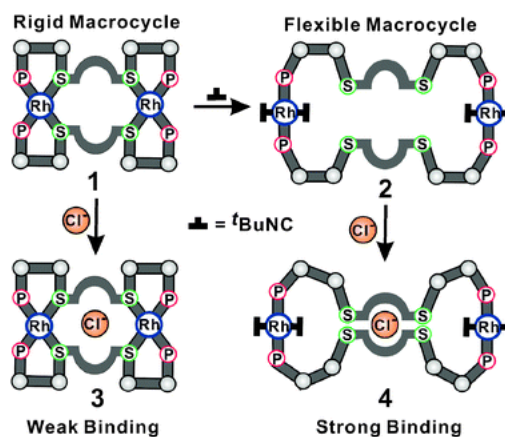


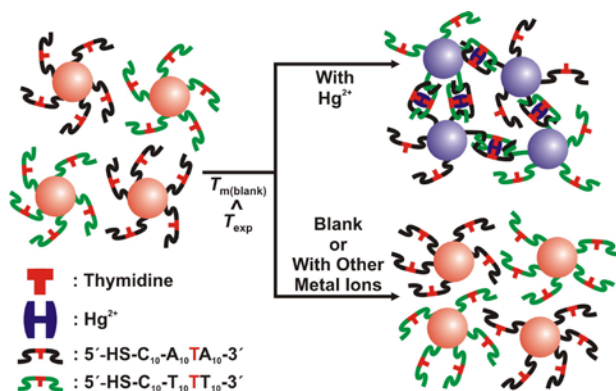
Figure 7. Strategy for allosteric control of the anion binding affinity of a macrocycle. The reaction of the macrocycle with a small molecule ($t\text{BuNC}$) at a metal-based regulatory site increases macrocycle size and changes its flexibility, leading to an increased affinity for chloride ions.

2.5 Colorimetric Detection of Mercuric Ion (Hg^{2+}) in Aqueous Media Using DNA-Functionalized Gold Nanoparticles

Mercury is a widespread pollutant with distinct toxicological profiles that exists in a variety of different forms: metallic, ionic, and as part of organic and inorganic salts and complexes. Solvated mercuric ion, Hg^{2+} , one of the most stable inorganic forms of mercury, is a caustic and carcinogenic material with high cellular toxicity. The most common organic source of mercury, methyl mercury, can accumulate in the human body through the food chain and can cause serious and permanent damage to the brain with both acute and chronic toxicity. Methyl mercury is generated by microbial biomethylation in aquatic sediments from water-soluble mercuric ion (Hg^{2+}). Therefore, the ability to routinely detect Hg^{2+} is central to the environmental monitoring of rivers and larger bodies of water and for evaluating the safety of the aquatically-derived food supply. Several methods for the detection of Hg^{2+} , which are based upon organic

fluorophores or chromophores, semiconductor nanocrystals, cyclic voltammetry, polymeric materials, proteins, and microcantilevers, have been developed. Colorimetric methods, in particular, are extremely attractive because they can be easily readout with the naked eye, in some cases at the point-of-use. Although there are now several chromophoric colorimetric sensors for Hg^{2+} , all of them are either limited with respect to sensitivity (current LOD = $\sim 1 \mu\text{M}$) and selectivity, kinetically unstable, or incompatible with aqueous environments.

Recently, DNA-functionalized gold nanoparticles (DNA-Au NPs) have been used in a variety of forms for the detection of proteins, oligonucleotides, certain metal ions, and other small molecules. DNA-Au NPs have high extinction coefficients (3 – 5 orders



Scheme 3. Colorimetric detection of mercuric ion (Hg^{2+}) using DNA-AuNPs.

of magnitude higher than organic dye molecules) and unique distance-dependent optical properties that can be chemically programmed through the use of specific DNA interconnects, which allows one, in certain cases, to detect targets of interest through colorimetric means. Moreover, these structures, when hybridized to complementary particles, exhibit extremely sharp melting transitions, which have been used to enhance the selectivity of detection systems based upon them. Using such an approach, one can typically detect nucleic acid targets in the low nanomolar to high picomolar target concentration range in colorimetric format. The ability to use such particles to detect Hg^{2+} in the nanomolar concentration range in colorimetric format would be a significant advance, especially when one considers that commercial systems for detecting Hg^{2+} rely on cumbersome ICP approaches not suitable for point-of-use applications. **Mirkin** developed a highly selective and sensitive colorimetric detection method for Hg^{2+} , which relies on thymidine- Hg^{2+} -thymidine coordination chemistry and complementary DNA-Au NPs with deliberately designed T-T mismatches.

When two complementary DNA-Au NPs are combined, DNA-linked aggregates are formed which can dissociate reversibly with a concomitant purple-to-red color change. For this novel colorimetric Hg^{2+} assay, however, **Mirkin** prepared two types of Au NPs (designated as probe A and probe B), each functionalized with different thiolated-DNA sequences (probe A: 5' HS- C10-A10-T-A10 3', probe B: 5' HS-C10-T10-T-T10 3'), which are complementary except for a single thymidine-thymidine mismatch (**Scheme 3**). Importantly, these particles also formed stable aggregates and exhibit the characteristic sharp melting transitions (FWHM < 1 °C) associated with aggregates formed from perfectly complementary particles, but with a lower T_m . Since it is known that Hg^{2+} will coordinate selectively to the bases that make up a T-T mismatch, it was hypothesized that Hg^{2+} would selectively bind to the T-T sites in the aggregates formed from mismatched strands and raise the T_m of the resulting structures. The analogous interaction with particle-free DNA leads to significant increases in T_m ($\Delta T_m = \sim 10 \text{ }^\circ\text{C}$).

The assay begins by adding an aliquot of an aqueous solution of Hg^{2+} at a designated concentration to a solution of the DNA-Au NP aggregates formed from probes A and B (1.5 nM each) at room temperature. Subsequently the solution is heated at a rate of 1 °C/min while its extinction is monitored at 525 nm where the Au NP probes exhibit the

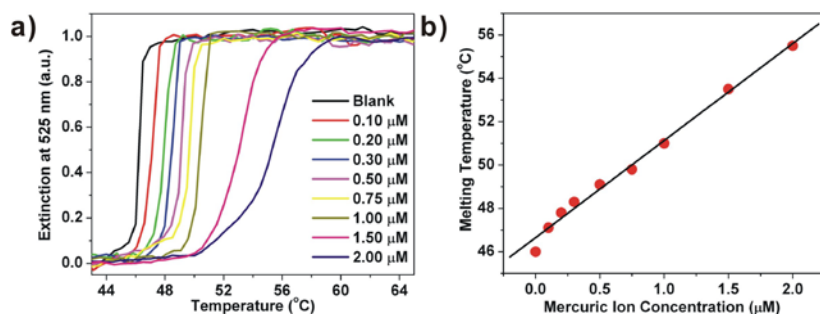


Figure 8. (A) Normalized melting curves of aggregates (probe A and B) with different concentrations of Hg^{2+} . (B) A graph of the T_m s for the aggregates as a function of Hg^{2+} concentration.

maximum intensity in the visible region of the spectrum. The T_m is obtained at the maximum of the first derivative of the melting transition. Without Hg^{2+} , the aggregates melt with a dramatic purple-to-red color change at about 46 °C. In the

presence of Hg^{2+} , however, the aggregates melt at temperatures higher than 46 °C due to the strong coordination of Hg^{2+} to the two thymidines that make up the T-T mismatch, thereby stabilizing the duplex DNA strands containing the T-T single base mismatches.

In order to evaluate the sensitivity of the assay, **Mirkin** tested different concentrations of Hg^{2+} from one stock solution. When an Hg^{2+} sample was mixed with the Au NP probe aggregate solution, there was no noticeable change under the reaction conditions described above. Once heated, however, the aggregates melted with a significant purple-to-red color change at a specific temperature (**Figure 8a**), which was linearly related to the concentration of Hg^{2+} over the entire concentration range studied (**Figure 8b**). The present limit of detection for this system is ~100 nM (= 20 ppb) Hg^{2+} (**Figure 8a**), which, to the best of **Mirkin's** knowledge, is the lowest ever reported for a colorimetric Hg^{2+} sensing system. Each 1 μM increase in concentration results in a ~5 °C increase in T_m , and provides an easy way of determining Hg^{2+} concentration. Three components of the assay contribute to its high sensitivity, selectivity, and quantitative capabilities: (1) the oligonucleotides, (2) the Au NPs, and (3) the oligonucleotide-nanoparticle conjugate. From the standpoint of the oligonucleotides, the chelating ability of the thymidines that form the mismatch in the oligonucleotide duplex is extremely selective for Hg^{2+} . It is known that two thymidine residues, when geometrically pre-organized in a DNA duplex, can behave as a chelate and form a tightly bound complex with Hg^{2+} . From the standpoint of the Au NPs, the high extinction coefficients of the Au NPs (~108 $\text{cm}^{-1} \text{M}^{-1}$ for 15 nm Au NPs) can act as an amplifier for the perturbation of the T_m upon binding Hg^{2+} , allowing ppb detection limits. Conventional chromogenic chemosensors have relatively low extinction coefficients (typically ~10⁵ $\text{cm}^{-1} \text{M}^{-1}$), which limit their sensitivity at best to the micromolar concentration range. Finally, the sharp, highly cooperative melting properties of aggregates made from oligonucleotide-Au NP conjugates enable one to clearly distinguish subtle T_m differences, providing a measure of the Hg^{2+} concentration over the 100 nM to low micromolar concentration range.

The selectivity of this system for Hg^{2+} was evaluated by testing the response of the assay to other environmentally relevant metal ions, including: Mg^{2+} , Pb^{2+} , Cd^{2+} , Co^{2+} , Zn^{2+} , Fe^{2+} , Ni^{2+} , Fe^{3+} , Mn^{2+} , Ca^{2+} , Ba^{2+} , Li^+ , K^+ , Cr^{3+} and Cu^{2+} (**Figure 9a**

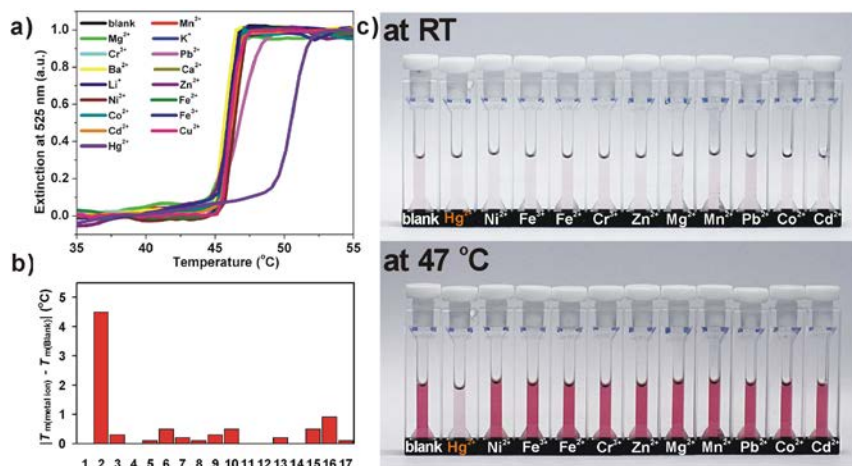


Figure 9. (A) Normalized melting curves of the aggregates (probe A and B) in the presence of these metal ions (each at 1 μM). (B) A graph showing the difference between the T_m of the aggregates of the blank and that of the aggregates with different metal ions: 1. blank; 2. Hg^{2+} ; 3. Li^+ ; 4. Cd^{2+} ; 5. Ca^{2+} ; 6. Ba^{2+} ; 7. Mn^{2+} ; 8. Mg^{2+} ; 9. Zn^{2+} ; 10. Ni^{2+} ; 11. Fe^{2+} ; 12. Co^{2+} ; 13. Fe^{3+} ; 14. K^+ ; 15. Cr^{3+} ; 16. Pb^{2+} ; 17. Cu^{2+} . (c) The color change of the aggregates (probe A and B, each at 1.5 nM) in the presence of various representative metal ions (each at 1 μM) at 47 $^{\circ}\text{C}$.

and **9b**) at a concentration of 1 μM . Only the Hg^{2+} sample shows a significantly higher T_m ($\Delta T_m = \sim 5$ $^{\circ}\text{C}$) compared to that of the blank. Indeed, at 47 $^{\circ}\text{C}$, only the aggregate solution containing Hg^{2+} is purple, while all the others have turned bright red. Pb^{2+} is the only other metal ion that influences the T_m of the aggregate but only by a negligible

amount ($\Delta T_m = \sim 0.8$ $^{\circ}\text{C}$). Importantly, this selectivity can be visualized with the naked eye (**Figure 9c**).

Because of the thiophilic nature of Hg^{2+} , the possibility was considered that it could be removing the thiolated oligonucleotides from the gold particle surface. This could result in non-uniformity of the assay and a potential loss of sensitivity and

Temperature	Portion	Mercuric Ion Concentration		
		0.5 μM	1 μM	2 μM
Room Temperature	In the Supernatant	2.1 ± 1.0	1.6 ± 1.3	1.8 ± 1.2
	On the Particles	68.0 ± 0.9	68.9 ± 1.8	68.1 ± 2.0
50 $^{\circ}\text{C}$	In the Supernatant	5.9 ± 0.2	6.0 ± 0.8	6.1 ± 1.3
	On the Particles	64.7 ± 1.1	64.1 ± 0.8	65.0 ± 2.2

Table 1. The number of fluorophore-labeled DNA strands per particle before and after being exposed to Hg^{2+} at room temperature or 50 $^{\circ}\text{C}$ for 8 hours.

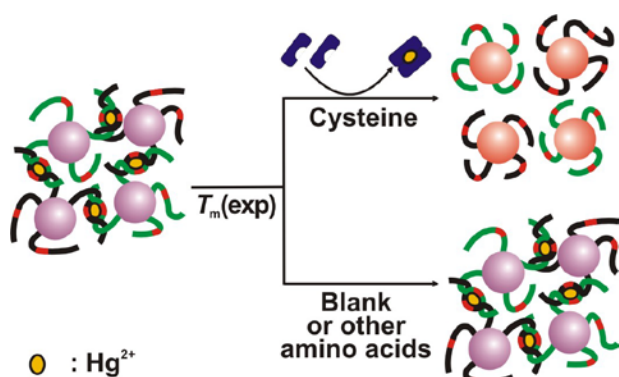
accuracy. In order to determine if this was occurring, fluorophore-labeled oligonucleotides were used to evaluate the number of DNA strands per particle at various Hg^{2+} concentrations (0.5, 1, and 2 μM over 8 h; oligonucleotide sequence: 5' HS-C10-A10-T-A10-(6-FAM) 3'). Significantly, Hg^{2+} showed no evidence of fluorophore quenching while the gold particle is an excellent quencher of fluorescence. Therefore, if the fluorophore-labeled oligonucleotides are removed from the particles they can be

easily identified and quantified by fluorescence spectroscopy. The coverage of DNA, at the start of the reaction, was determined to be ~70 strands per particle using published methods. The mercuric ion, regardless of the concentration studied, has very little effect on the surface coverage of the DNA (**Table 1**). Even at elevated temperature (50 °C), there is less than 10% loss of DNA from the surface of the particle even after prolonged heating (8 hours) (**Table 1**). This suggests that the particle probes will be stable over any reasonable assay conditions.

In conclusion, **Mirkin** developed a colorimetric method to detect Hg^{2+} in aqueous media with very high selectivity and sensitivity using DNA-Au NPs. This method requires neither enzymes nor specialized equipment other than a temperature control unit. The concentration of Hg^{2+} can be determined by the color change of the solution at a given temperature, or the melting temperature (T_m) of the DNA-Au NP aggregates. Unlike most of the chemosensors for Hg^{2+} which have been evaluated in organic media or organic-aqueous mixtures owing to their low water-solubility, the high water solubility of the oligonucleotide-modified gold nanoparticle probes allow this assay to be performed in aqueous media without the need for organic co-solvents. Significantly, in principle this method can be used to detect other metal ions by substituting the thymidine with synthetic artificial bases which selectively bind other metal ions.

2.6 A DNA-Gold Nanoparticle Based Colorimetric Competition Assay for the Detection of Cysteine

During the early years of the MURI, **Mirkin** also developed a highly sensitive and selective colorimetric detection method for cysteine. This method was based upon oligonucleotide-functionalized gold nanoparticle probes that contain strategically placed



Scheme 4. Colorimetric detection of cysteine using DNA-AuNPs.

T-T mismatches complexed with Hg^{2+} . This assay relies upon the distance-dependent optical properties of gold nanoparticles, the sharp melting transition of oligonucleotide-linked nanoparticle aggregates, and the very selective coordination of Hg^{2+} with cysteine. The concentration of cysteine can be determined by monitoring, with the naked eye or a UV-vis spectrometer, the temperature at which the purple-to-red color change associated with aggregate dissociation takes place. This assay does not utilize organic co-solvents, enzymatic reactions,

light-sensitive dye molecules, lengthy protocols, or sophisticated instrumentation, thereby overcoming some of the limitations of more conventional methods.

As a sulfur-containing amino acid, cysteine plays a crucial biological role in the human body by providing a modality for the intramolecular crosslinking of proteins through disulfide bonds to support their secondary structures and functions. It is also a potential neurotoxin, a biomarker for various medical conditions, and a disease-associated physiological regulator. A variety of methods for detecting cysteine, such as fluorometry based upon fluorescent dyes, electrochemical voltammetry and fluorescence-coupled HPLC techniques, have been developed. Most of these methods, however, require complicated instrumentation, involve cumbersome laboratory procedures and are low throughput, which limits the scope of their practical applications. Recently,

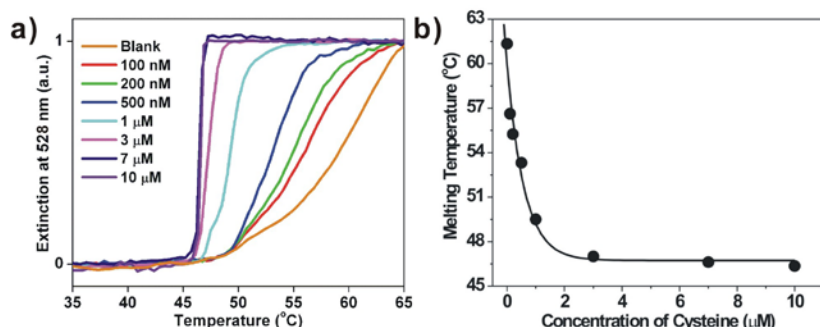


Figure 10. (A) Normalized melting transitions of DNA-Au NP/Hg²⁺ complex aggregates at different concentrations of Hg²⁺. (B) T_m s of the melting transitions in (A) as a function of Hg²⁺ concentration.

significant advances have been made in the development of chromophoric colorimetric sensors for detecting cysteine, which have attracted attention due to their easy readout (often with the naked eye) and potential for high throughput formats. However, these systems are also

limited with respect to sensitivity (limit of detection (LOD) $\geq \sim 1 \mu\text{M}$), and, in certain cases, not stable or functional in aqueous environments.

Assays based upon oligonucleotide-gold nanoparticle conjugates (DNA-Au NPs) are emerging as alternatives to more conventional chromogenic sensors. The DNA-Au NPs are attractive as colorimetric probes due to their intense optical properties, chemical tailorability, distance- and aggregate size-dependent optical properties, unusual hybridization and melting properties, and chemical stability. Thus far, DNA-Au NPs have been used to develop assays for a wide variety of analytes, including proteins, oligonucleotides, certain metal ions and other small organic molecules. Assays for cysteine based upon unmodified Au nanoparticles that rely on the non-selective adsorption of cysteine on the surface of the nanoparticle to effect aggregation and a colorimetric change have been developed. However, while conceptually simple, they lack selectivity and have relatively high LODs ($\geq \sim 7 \mu\text{M}$).

Building off this work, **Mirkin** developed a new class of assays based upon nanoparticle aggregates formed from DNA duplex interlinks. These DNA-linked Au NP network structures have shown promise for detecting important nucleic acid analytes with single mismatch selectivity, probing Hg²⁺ ion at nM levels, identifying triplex promoters, screening duplex DNA intercalators, monitoring enzyme activity and inhibition in real time, and screening the sequence selectivity of DNA-binding molecules in a high throughput manner. The premise behind these assays is that perturbation of the DNA links holding the particles within the aggregates together will lead to a change in the melting temperature (T_m) of the aggregates and therefore the colorimetric transition that takes place when the particles disperse. The Hg²⁺ example is particularly interesting

because it is based upon the concept that a T-T mismatch is very selective for Hg^{2+} binding. Indeed, when Hg^{2+} binds to the DNA it can increase the T_m by $\sim 10^\circ\text{C}$. **Mirkin's** novel cysteine assay relies on this observation. Au NP networks interconnected



Figure 11. (A) Normalized melting transitions of DNA-Au NP/ Hg^{2+} complex aggregates at different concentrations of Hg^{2+} . (B) T_m s of the melting transitions in (A) as a function of Hg^{2+} concentration.

they rapidly formed aggregates through DNA-hybridization (confirmed by melting analyses) and turned purple. In general, DNA-Au NP aggregates that contain a single base mismatch dissociate at a temperature lower than that of perfectly complementary particles, with a concomitant purple-to-red color change. However, it is known that aggregates linked by DNA strands with T-T mismatches will selectively bind Hg^{2+} and form aggregates that were substantially more stable than the Hg^{2+} -free structures. This increased stability was reflected in the T_m values, with the T_m of the mercuric ion-bound structure being shifted $+10^\circ\text{C}$ compared to the mercuric ion-free structure. When cysteine was added to the solution containing the purple aggregates linked by DNA with Hg^{2+} complexed T-T mismatches, the mercury was sequestered from the aggregate through cysteine complexation, which lowers the T_m of the aggregate and the temperature at which the purple-to-red color change occurs.

The limit of detection and the dynamic range of the assay were determined by **Mirkin** by preparing and studying aqueous cysteine solutions at concentrations ranging

with duplex DNA with strategically placed Hg^{2+} -complexed thymidine-thymidine (T-T) mismatches (DNA-Au NP/ Hg^{2+} aggregates, **Scheme 4**) were intentionally prepared by **Mirkin**. The cysteine analyte can bind the mercuric ions and remove it from the network structure, thereby lowering the temperature at which the DNA duplexes dissociate and the corresponding purple to red color change takes place. Cysteine can be detected at concentrations as low as a 100 nM using this assay in a colorimetric format.

In a typical assay, two sets of Au NP probes, functionalized with different oligonucleotide sequences (probe A: 5' HS- C10-A10-T-A10 3'; probe B: 5' HS-C10- T10-T- T10 3'), were prepared using published procedures and suspended in MOPS buffer (100 mM MOPS, pH 7.5) by **Mirkin**. When aliquots of the red solutions containing the two Au NP probes were combined,

from 50 nM to 10 μM . In general, when an aliquot of the solution containing cysteine was combined with the solution containing the DNA-Au NP/ Hg^{2+} aggregates and the mixture brought to a cysteine concentration that fell within the range cited above, no

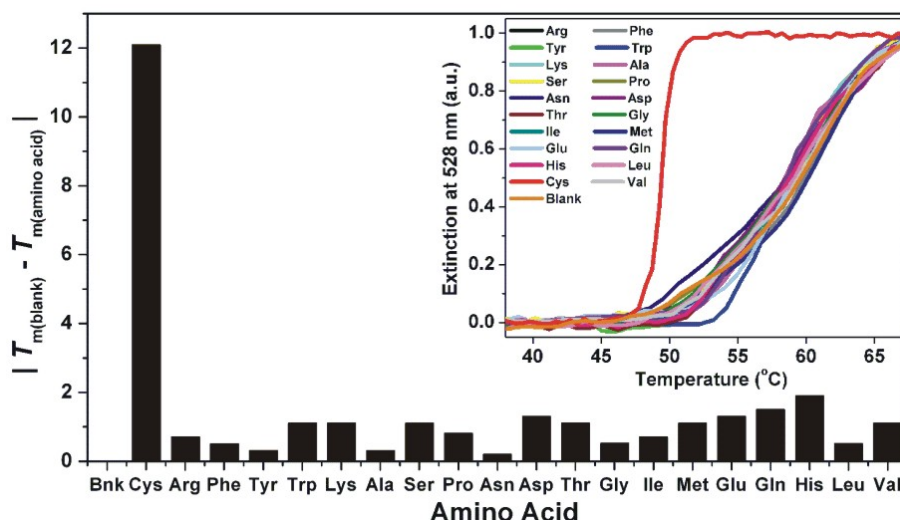


Figure 12. The difference of the T_m s of the blank and the amino acid samples (each at 1 μM), and their normalized melting profiles (inset).

change in color was observed at room temperature. Upon heating, however, the aggregates dehybridized with a concomitant purple-to-red color change. The melting transition was obtained by heating the aggregates at a rate of 1 $^{\circ}\text{C}/\text{min}$ while monitoring the extinction at 528 nm (**Figure 10a**), and the T_m was determined from the maximum of the first derivative of the melting transition in the visible region of the spectrum. Importantly, the observed T_m inversely correlates with the concentration of cysteine over the entire range of detectable cysteine concentrations studied (**Figure 10a** and **10b**). Note that at higher concentrations, the dependence of the T_m on the cysteine concentration decreases because most of the Hg^{2+} has been removed from the aggregate. The LOD for this system is ~ 100 nM for cysteine. Over the region of highest sensitivity (left part of the curve in **Figure 10b**), each 100 nM increase in cysteine concentration results in a ~ 0.7 $^{\circ}\text{C}$ decrease in T_m . This trend is consistent up to a cysteine concentration of 2 μM , allowing one to measure cysteine concentrations in a quantitative way. Since the total concentration of Hg^{2+} at the

Temperature	Cysteine Concentration (μM)		
	0	1	10
25 $^{\circ}\text{C}$	126.2 ± 1.3	$1.21.7 \pm 4.5$	118.5 ± 5.3
50 $^{\circ}\text{C}$	117.3 ± 2.6	112.5 ± 5.4	106.2 ± 11.2

Table 2. The average number of fluorophore-labeled DNA strands per particle before and after exposure to cysteine for 1 hour at 25 $^{\circ}\text{C}$ or 50 $^{\circ}\text{C}$.

In order to determine the selectivity of this assay, **Mirkin** studied its colorimetric response to the other 19 essential amino acids at a concentration of 1 μM (**Figure 11**). The color of the aggregate solutions in the presence of these amino acids remained unchanged at 50 $^{\circ}\text{C}$, the temperature at which the colorimetric transition takes place in the presence of cysteine (**Figure 11**). The melting behavior of this system was then

change in color was observed at room temperature.

Upon heating, however, the aggregates dehybridized with a concomitant purple-to-red color change. The melting transition was obtained

by heating the aggregates at a rate of 1 $^{\circ}\text{C}/\text{min}$ while monitoring the extinction at 528 nm (**Figure 10a**), and the T_m was determined from the maximum of the first derivative of the melting transition in the visible region of the spectrum. Importantly, the observed T_m inversely correlates with the concentration of cysteine over the entire range of detectable cysteine concentrations studied (**Figure 10a** and **10b**). Note that at higher concentrations, the dependence of the T_m on the cysteine concentration decreases because most of the Hg^{2+} has been removed from the aggregate. The LOD for this system is ~ 100 nM for cysteine. Over the region of highest sensitivity (left part of the curve in **Figure 10b**), each 100 nM increase in cysteine concentration results in a ~ 0.7 $^{\circ}\text{C}$ decrease in T_m . This trend is consistent up to a cysteine concentration of 2 μM , allowing one to measure cysteine concentrations in a quantitative way. Since the total concentration of Hg^{2+} at the start of the experiment was 1 μM , one can conclude that the 2 μM concentration value for saturation reflects the formation of the aggregate-free 2:1 cysteine: Hg^{2+} adduct.

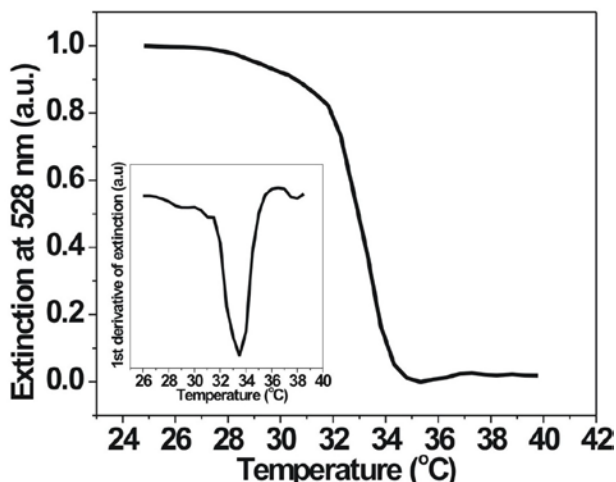


Figure 13. Melting profile of DNA-Au NP probes (DNA a) hybridized to the oligonucleotide (DNA b) on the Codelink Slide. The T_m is determined to be 33.5 °C from the minimum of the first derivative of the melting profile (inset).

allow one to monitor very subtle differences in T_m affected by the cysteine analyte and therefore provide a quantitative measure of the cysteine concentration. Finally, the high selectivity for and tight binding of cysteine to Hg^{2+} at the T-T mismatch sites in comparison to the other amino acids leads to an assay with high specificity. Interestingly, methionine, the other sulfur-containing amino acid, did not cause a significant change in T_m . The binding affinity of Hg^{2+} for the thiol in cysteine must be substantially greater than that for the thioether in methionine. In addition, Hg^{2+} is known to have an affinity for certain N-type ligands, potentially including basic amino acids such as histidine or lysine. However, in this system if there is such an interaction it is not significant enough to affect the assay. The T-T mismatch site appears to be a strong enough Hg^{2+} binder to effectively compete against all of the amino acids studied other than cysteine.

It is well known that thiolated molecules such as DTT (dithiothreitol) remove thiolated oligonucleotides from Au surfaces. Therefore, the possibility of such displacement by cysteine through a ligand exchange process was considered, which could result in irregular functionality of the

evaluated in the presence of each amino acid (**Figure 12, inset**). Only cysteine exhibits a significant perturbation on the Hg^{2+} -duplex interconnects, demonstrating the high selectivity of this system (**Figure 12**).

There are three factors responsible for the high sensitivity, selectivity, and quantitative output of this assay. First, the high extinction coefficients of the gold nanoparticle-oligonucleotide conjugates ($8.1 \times 10^8 \text{ cm}^{-1} \text{ M}^{-1}$ for 20 nm Au NPs) allows one to monitor the changes in duplex T_m at lower concentrations than one can monitor with conventional absorbance-based chromophores (extinction coefficients $\sim 10^4 - 10^5 \text{ cm}^{-1} \text{ M}^{-1}$). The sharp melting transitions for aggregates formed from Au NPs

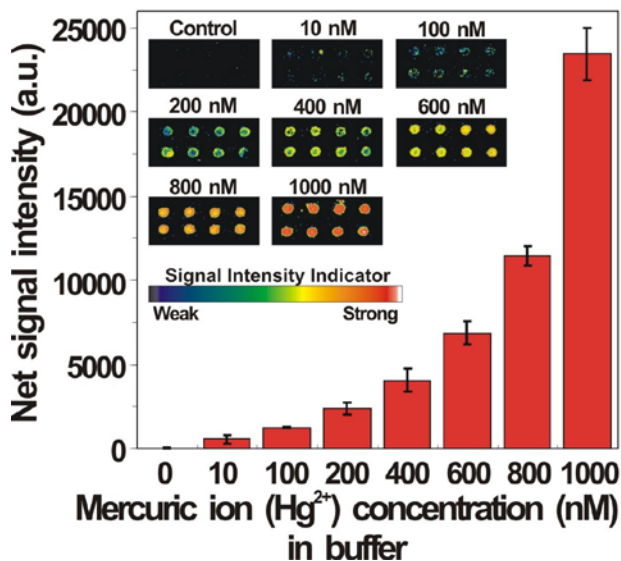


Figure 14. Average scanometric signal intensity as a function of the Hg^{2+} concentration in buffer. The corresponding scanometric signal images are shown as an inset. The spot diameter is $\sim 200 \mu\text{m}$.

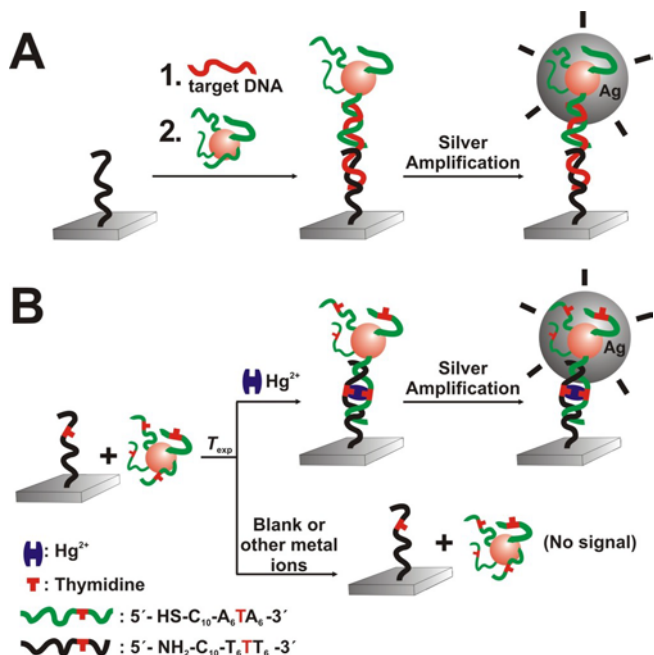
NP probes and impede assay performance. To verify the stability of the DNA-Au NPs toward cysteine, the number of oligonucleotides bound to the nanoparticle probe was determined using fluorescence spectroscopy before and after conducting the assay. In this study, **Mirkin** used a thiol- modified oligonucleotide sequence labeled with a fluorophore (F-probe A, 5' HS-C10-A10-T-A10- (6-FAM) 3') to functionalize Au NPs (20 nm in diameter). The DNA-Au NPs labeled with a fluorophore were incubated with different concentrations of cysteine (0, 1, and 10 μM over 1 hour at 25 $^{\circ}\text{C}$ and 50 $^{\circ}\text{C}$), and the number of DNA strands before and after incubation with cysteine determined by measuring the fluorescence from the DNA released by DTT. Based on this surface loading assay it was determined that there were approximately 126 oligonucleotides per as-prepared particle. After soaking in a 10 μM aqueous solution of cysteine for 1 hour at room temperature, 90% of the oligonucleotides remained on the particles (113 strands/particle, Table 2). Even at elevated temperatures (50 $^{\circ}\text{C}$), the average number of DNA strands per particle was about 106 (Table 2), indicating that the probes survived the conditions of the assay.

In conclusion, **Mirkin** developed a new type of rapid, highly selective, and sensitive colorimetric assay for detecting cysteine using gold nanoparticle-oligonucleotide conjugates was developed. This assay is based on the thiophilicity of Hg^{2+} , and the unique optical properties and sharp melting properties of DNA-Au NPs in a competition assay format. Importantly, the assay is easily read out with the naked eye or a UV-vis spectrometer by monitoring the temperature at which the purple-to-red color change takes place, thus providing a quantitative measurement of cysteine concentration in a high throughput manner. The limit of detection (LOD) is 100 nM. The assay is particularly attractive because it does not rely on organic co-solvents, enzymatic reactions, light-sensitive dye molecules, lengthy protocols, and sophisticated instrumentation.

2.7 Chip-Based Scanometric Detection of Mercuric Ion Using DNA-Functionalized Gold Nanoparticles

In separate but related work, **Mirkin** developed a scanometric detection method for nucleic acid targets that relies on DNA-Au NPs to detect oligonucleotides. This assay utilizes the catalytic properties of the nanoparticles in a subsequent amplification event to effect the reduction of Ag^{+} in the presence of hydroquinone (**Scheme 5A**). One simply needs to measure the scattered light from the resulting silver spots to quantify the amount of an oligonucleotide target present. **Mirkin** hypothesized that one could utilize a variant of the approach to create a high-sensitivity, chip-based assay for Hg^{2+} by using probes capable of hybridizing with surface immobilized oligonucleotides to form duplexes with T-T mismatches. Hg^{2+} binding to these sites would create more stable duplex structures and raise the temperature associated with dehybridization (**Scheme 5B**). Therefore, a stringency wash followed by silver amplification could potentially lead to a very high sensitivity and convenient assay for Hg^{2+} . **Mirkin** evaluated the performance of this novel assay and show that one can detect Hg^{2+} down to the EPA-acceptable concentration (10 nM, or 2 ppb) in drinkable water.

In a typical experiment, **Mirkin** spotted a glass slide with an oligonucleotide sequence (DNA b: 5' H2N-C10- T13 3') capable of hybridizing with a nanoparticle



Scheme 5. Colorimetric detection of cysteine using DNA-AuNPs.

Hg^{2+} was incubated with DNA b on a surface for 30 min. The final concentration of Hg^{2+} in the incubation mixtures was adjusted from 0 to 1 μM (0, 10, 100, 200, 400, 600, 800, and 1000 nM). The chip was washed under stringency and enhanced with the Ag^{+} /hydroquinone solution. After silver enhancement, the scattered light from the silver spots was measured with a Verigene Reader. Significantly, signal intensity proportionally correlates with Hg^{2+} concentration (**Figure 14**). The LOD under these conditions was determined to be 10 nM (= 2 ppb), which is comparable to the LOD of the most sensitive assays based upon fluorescent dyes (LOD = ~10 nM).

In addition to sensitivity, **Mirkin** investigated the selectivity of this assay by comparing the scanometric response in the presence of Hg^{2+} and other metal ions at a concentration of 1 μM . **Mirkin** first studied the scanometric response in the presence of each metal ion at 1 μM concentration (**Figure 15**). **Mirkin** studied 15 different metal ions in this fashion and discovered that the assay exhibits very high selectivity for Hg^{2+} in the presence of each of them. First row transition metal ions (Cr^{3+} , Mn^{2+} , Fe^{2+} , Fe^{3+} , Co^{2+} , Ni^{2+} , Cu^{2+}), common group 12 metal ions (Zn^{2+} , Cd^{2+}), group 1 and 2 metal ions (Li^{+} , Ba^{2+} , K^{+} , Ca^{2+} , Mg^{2+}), and Pb^{2+} , a common environmental pollutant, were all investigated. Under stringency conditions, only the Hg^{2+} showed a significant response. In all

probe (1 nM, 20 nm Au NP; DNA a: 5'-HS-C₁₀-A₆-T-A₆-3') to form a duplex with a single T-T mismatch (**Scheme 5B**). The T_m of this structure, determined by melting analysis, is 33.5 $^{\circ}\text{C}$ at 0.10 M NaNO_3 (**Figure 13**). Based upon this experiment, the optimum stringency conditions in aqueous media were determined to be 34 $^{\circ}\text{C}$ and 0.10 M NaNO_3 . Once the optimum stringency conditions were determined, **Mirkin** evaluated the effect of Hg^{2+} on the stability of the duplex structure under stringency conditions. In a typical experiment, a mixture of DNA-Au NP probes (DNA a) with

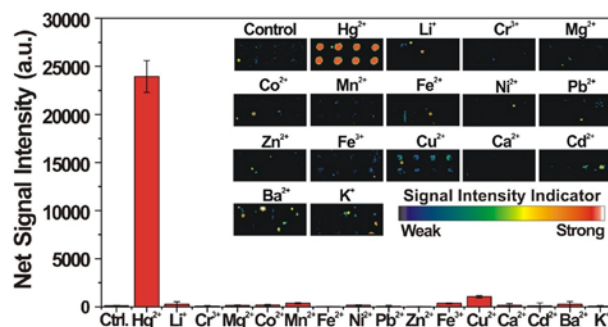


Figure 15. Scanometric response of the assay in the presence of various metal ions (M^{x+} , 1 μM). The control (ctrl) does not contain any metal ions. Note that only Hg^{2+} shows intense signals with very high selectivity. The spot diameter is ~200 μm .

cases, the Hg^{2+} exhibited a 25-800-fold stronger signal than that of any of the other metal ions (**Figure 15**). **Mirkin** attributed this high selectivity to two parameters: (1) the sharp melting transitions associated with nanoparticle probe duplex structures, which lead to high discrimination of single base mismatches in the scanometric assay and (2) the selective binding of the T-T mismatch to Hg^{2+} . **Mirkin** and other researchers have demonstrated that the T-T mismatch is very selective for binding Hg^{2+} in a variety of DNA- based Hg^{2+} sensing systems based upon DNazymes, molecular beacons, DNA-polymer mixtures, and DNA-nanoparticle conjugates.

Finally, **Mirkin** explored the capability of the assay to detect Hg^{2+} in natural media using water from Lake Michigan. The original concentration of Hg^{2+} in the lake water was determined to be ~ 6 nM ($=1.2$ ppb) by ICP-MS, which is below the LOD of the assay. $[\text{Hg}(\text{ClO}_4)_2]$ was added to a 10-mL aliquot of lake water and diluted to create standard solutions of varying Hg^{2+} concentration. Under these conditions, the assay reliably predicted the concentration of each solution over the “0”-1 μM range. Importantly, the assay can clearly distinguish 10 nM Hg^{2+} from the lake water control with no added Hg^{2+} , demonstrating the versatility of the assay for detecting Hg^{2+} even in natural media (**Figure 16**).

To conclude, **Mirkin** developed a highly sensitive and selective chip-based scanometric assay for the detection of Hg^{2+} using the sharp melting properties of DNA-Au NPs and the selective T-T coordination chemistry for Hg^{2+} . This assay can selectively identify Hg^{2+} even in the presence of 15 other environmentally and physiologically relevant metal ions. The LOD of this assay is 10 nM (2 ppb) for Hg^{2+} in buffer and natural media, which is the maximum allowable level of Hg^{2+} in drinkable water defined by the EPA. This assay does not rely on organic co-solvents, enzymatic reactions, or complicated instrumentation, pointing toward potential point-of-use applications. The results of the assay at Hg^{2+} concentrations higher than 600 nM can be read out with the naked eye or a flatbed scanner. At low concentrations, a Verigene Reader, a simple light scattering device, can be used to detect and quantify Hg^{2+} using this assay.

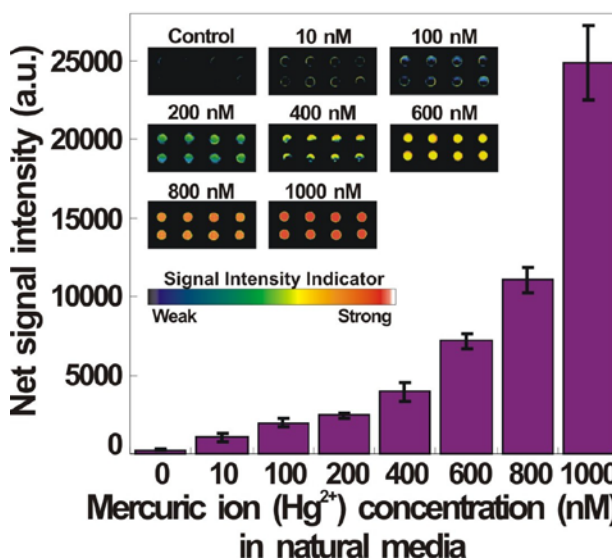


Figure 16. Average scanometric signal intensity as a function of the Hg^{2+} concentration in natural media. The corresponding scanometric signal images are shown as an inset. The spot diameter is ~ 200 μm .

2.8 Colorimetric Cu^{2+} Detection Using DNA Modified Gold Nanoparticle Aggregates as Probes and Click Chemistry

Copper is a transition metal essential for life. At elevated concentrations, however, it is highly toxic to organisms such as algae, fungi and many bacteria, and in humans, may adversely affect the gastrointestinal, hepatic and renal systems. As such, the detection and measurement of copper ions in water has become increasingly important,

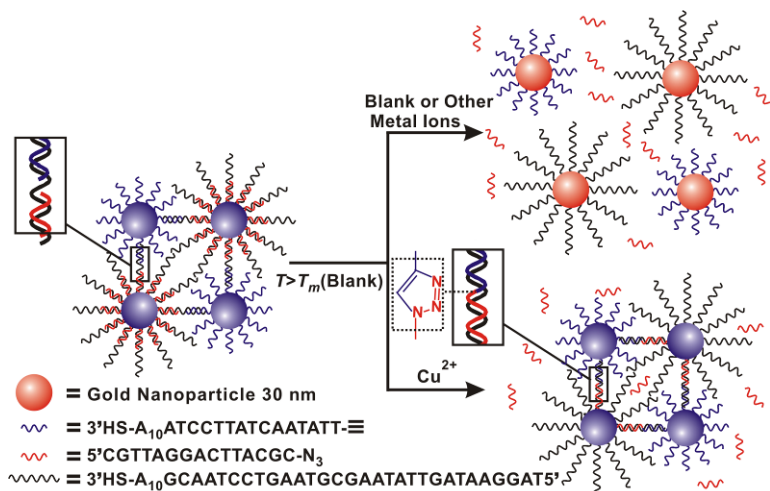


Figure 17. Schematic illustration representing the aggregation and dissociation of the gold nanoparticle probes used in the colorimetric detection of copper ions.

especially in point-of-use formats. Several methods exist for the detection of Cu^{2+} ions, including those based on organic dyes,

semiconductor nanocrystals, spectroscopy, and cyclic voltammetry. The read out mechanisms for these methods, however, often require sophisticated

instrumentation. In contrast, colorimetric methods are extremely attractive for point-of-

use applications, since they can be easily interpreted with the naked eye or low-cost portable instruments.

DNA gold nanoparticle (Au NP) conjugates have been used in a variety of detection formats for DNA, proteins, metal ions, enzyme inhibitors, small molecules, and intracellular mRNA. DNA Au NPs have high extinction coefficients (about 4 orders of magnitude greater than typical organic dyes) and unique distance-dependent plasmonic properties. When hybridized to complementary particles, DNA Au NPs turn from red to purple, and their aggregates exhibit extremely sharp melting transitions that make them useful for the colorimetric detection of oligonucleotides. These optical and melting properties have also been utilized in mercuric ion detection, where deliberately designed T – T mismatches in the interparticle oligonucleotide duplexes selectively complex Hg^{2+} via coordination chemistry. The formation of the T – Hg^{2+} – T coordination complexes raises the T_m of the polymeric aggregates, so the solution color measured as a function temperature can be used to determine Hg^{2+} concentration.

Mirkin developed a colorimetric method for the detection of Cu^{2+} ions based on densely functionalized DNA Au NP conjugates and click chemistry. This new approach relies on the ligation of two 15 base pair (bp) oligonucleotide strands within polymeric aggregates of the DNA Au NPs (**Figure 17**). The oligonucleotide strands were terminated in a hexynyl or azide group, allowing them to be ligated into a 30 bp strand with click chemistry. **Mirkin** hypothesized that this ligation would raise the T_m of the aggregate in proportion to the amount of copper ion present after a given time (a kinetic endpoint),

which could be monitored by UV-vis spectroscopy or the naked eye. The use of click chemistry and DNA Au NPs confers three specific advantages that the previous Au NP-based systems lacked in whole or in part. First, this approach uses the oligonucleotides as



Figure 18. A photograph of the DNA Au NPs at 55 °C in the presence of different metal ions after ligation.

detection systems, this method does not require labile reactive groups or long incubation times due to the robustness of the alkyne and azide functionalities and the fact that those groups are templated together for optimal reactivity via oligonucleotide hybridization, respectively. Taken together, these advantages make this assay simple and robust, and therefore promising for on-site water testing. As such, the strategy presented in this work represents a promising new addition to the growing library of NP-based probes for protein, nucleic acid, metal ion, and small molecule detection.

a template to align the alkyne and azide groups for optimal reactivity. Second, the sharp melting properties of the DNA Au NPs allow one to distinguish subtle difference in T_m , allowing for Cu^{2+} quantification. Finally, the alkyne and azide groups are robust, and their cyclization can be catalyzed specifically (almost exclusively) by copper ions.

Based on these concepts **Mirkin** developed a colorimetric copper ion detection system with high selectivity and sensitivity (**Figure 18**). The concentration of Cu^{2+} can be determined by the change in solution color at a given temperature, or through a measurement of the melting temperature of the DNA Au NP aggregates. In contrast to other Au NP based

2.9 Docking in Metal-Organic Frameworks

Biological systems use many “architectural domains” to carry out specific tasks leading to complex functions. This concept is useful because such domains operate independently,

yet they are connected.

Although the design of synthetic materials that ‘mimic’ biology is decidedly a futile exercise,

Stoddart

believes that “concept transfer” from biology is a more viable

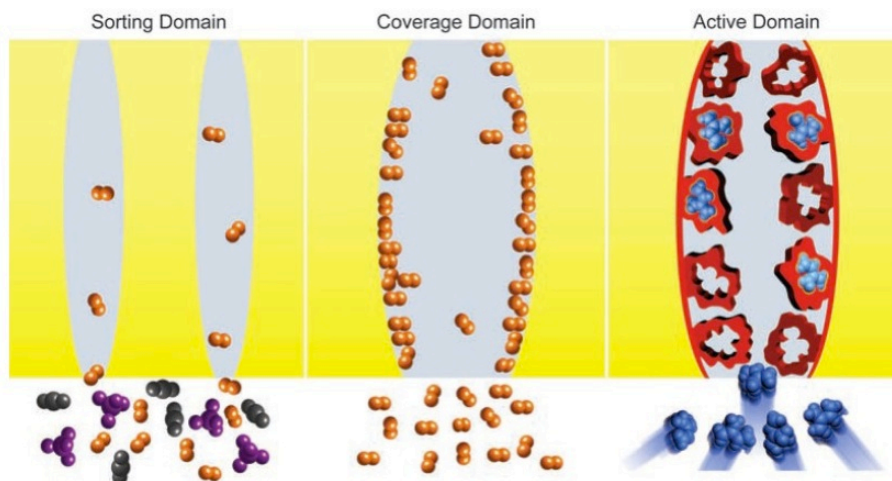


Figure 19. Classification of the different porous domains in metal-organic frameworks.

strategy toward achieving materials with higher complexity. Recently, he and his group along with **Hupp, Mirkin, Ratner, and Nguyen** focused their attention on the design and synthesis of porous crystals composed of several architectural domains, one of which is capable of docking molecules in a manner akin to the well-known molecular docking of drug molecules within protein receptors.

Stoddart's design takes advantage of the emerging chemistry of metal-organic frameworks (MOFs), which have been used effectively to assemble components with

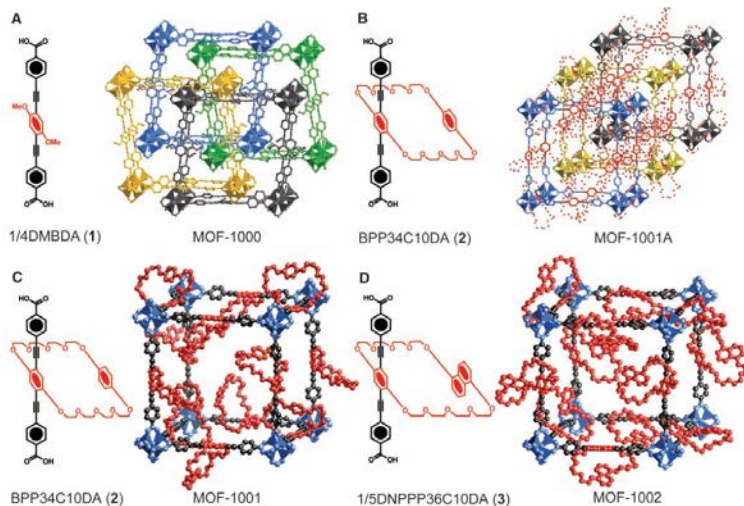


Figure 20. Ball-and-stick drawings of single crystal structures of (A) MOF-1000, (B) BORG-1A, (C) BORG-1, (D) BORG-2, and their corresponding organic struts.

distributed by virtue of their weak interactions with adsorption sites covering the struts and joints (*coverage domain*). However, the synthesis of more complex MOFs with more than two domains remains unexplored. **Stoddart** has shown how molecular recognition components, much used in supramolecular chemistry, can be integrated in a modular fashion into struts of MOFs, thereby creating recognition sites into which incoming guests will dock in a highly specific manner with stereoelectronic control (*active domain*). In essence, the third domain combines shape, size, and electronic elements for the recognition of incoming guests, and brings order to otherwise highly disordered guests in conventional MOFs. Thus, this chemistry presents a new class of MOFs that are beyond open reticulated geometries (BORGs).

Specifically, **Stoddart** used the primitive cubic topology of the archetypical MOF-5, in which benzene struts are joined by $\text{Zn}_4\text{O}(\text{CO}_2)_6$ cluster joints, as the target for his design. Initially, he demonstrated the feasibility of using the long 1/4DMBDA (1) to make MOF-1000, which has MOF-5 topology, albeit quadruply interpenetrated (**Figure 20A**). This approach was extended to the more complex struts, BPP34C10DA (2) and 1/5DNPPP36C10DA (3), which are known to act as electron-rich receptors for electron-deficient substrates, to make the corresponding BORG-1A, BORG-1 and BORG-2 (**Figure 20 B to D**). **Stoddart** further showed that, indeed, each of the crown ether receptors in BORG-1 is addressable as evidenced by the docking of the paraquat dication (PQT^{2+}) at every one of the receptor sites. In contrast to known MOFs, where the frameworks are used mainly as passive platforms for the adsorption of gases and

simple constitutions – specifically, organic struts and inorganic joints – into three-dimensionally ordered structures. The vast majority of porous MOFs prepared thus far can be regarded as having two important architectural domains (**Figure 19**): (1) the pore aperture which is responsible for the shape- and size-selective binding of incoming molecules (*sorting domain*), and (2) the internal surface of the pores onto which gases such as hydrogen and methane can be compacted and randomly

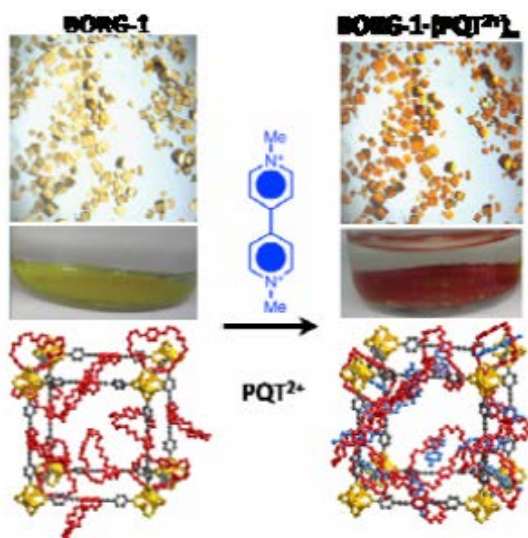


Figure 21. Docking of PQT^{2+} in metal-organic frameworks.

confirmed the practicality of creating BORGs using this synthetic protocol.

Struts 2 and 3, containing 34- and 36-membered polyether rings, which have been extensively used as receptors for a wide range of electron-deficient substrates, are ideally suited as molecular recognition modules for making BORGs. Strut 2 was prepared by means of a convergent synthetic approach, and used under conditions similar to those employed in the synthesis of MOF-1000 to give BORG-1A and BORG-1. The crystal structure of BORG-1A is a triply interpenetrating framework (**Figure 20B**), while that of BORG-1 is the corresponding noninterpenetrating form (**Figure 20C**); both have the MOF-5 type topology. Furthermore, **Stoddart** extended the methodology to the synthesis of BORG-2 (**Figure 20D**) by using the 1,5-dioxynaphthalene-containing strut 3, which was produced via a divergent synthetic route. Single crystal X-ray diffraction studies indicate that BORG-2 shares an identical cubic backbone with BORG-1, affirming the generality of such a methodology of building a variety of crystalline structures with long struts capable of molecular recognition.

The BORGs presented here combine the precise positioning of the

molecules, BORG-1 not only has active components in precise recognition sites but also, by virtue of the openness of its structure, allows substrates to diffuse freely from solution, through the pores, and finally dock at these active domains.

Crystals of MOF-1000 (**Figure 20A**) were obtained by mixing a solution of strut 1 and $\text{Zn}(\text{NO}_3)_2 \cdot 4\text{H}_2\text{O}$, in *N,N*-diethylformamide (DEF) using conditions previously employed in the synthesis of MOF-5. Its crystal structure displays the same structural topology as does MOF-5. It is four-fold interpenetrated because of the length and slender nature of the strut. The distance between the two carbon atoms from the carboxylate groups is 19.3 Å. Successful crystallization of MOF-1000, however,

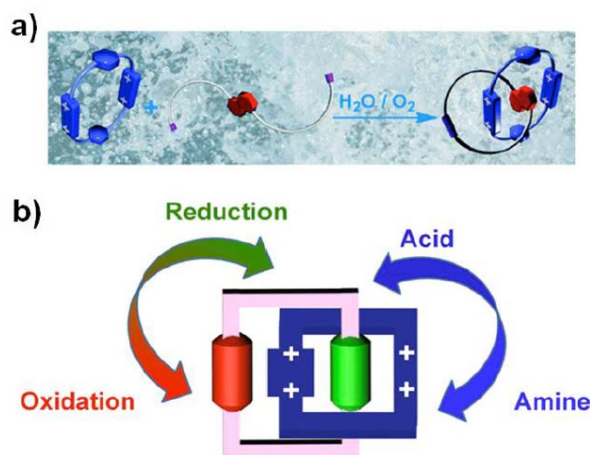


Figure 22. a) Graphical representation of the template-directed synthesis of a [2]catenane in water employing the hydrophobic effect as a major driving force behind the formation of a host-guest inclusion complex prior to the final catenation. b) Graphical representation of a dual-switchable catenane operated in water. Redox chemistry stimulates the circumrotation of the the ring bearing red and green stations, while acid/base chemistry drives the circumrotation of the blue ring.

active domains with docking as an expression of molecular recognition. This property was revealed by examining the molecular recognition behavior of the macrocyclic polyethers **2** and **3** as docking sites. When BORG-1 crystals were introduced into a saturated solution of PQT·2PF₆ in Me₂CO, the crystals immediately turned red (**Figure 21**), a typical behavior for this binding event that indicates significant charge-transfer interactions between PQT²⁺ and the crown ether rings. This observation points to the formation of BORG-1 pseudorotaxanes by threading of PQT²⁺ through the middle of the crown ether. The reversibility of such a process was confirmed by the reappearance of the original light yellow color upon rinsing with Me₂CO. Remarkably, the complexed BORG-1 maintained the original high crystallinity of the parent framework, as confirmed by their coincident powder X-ray diffraction (PXRD) patterns. These results show clearly that specific stereoelectronic host-guest interactions, rather than just simple diffusion and adsorption, are responsible for the formation of the BORG-1 pseudorotaxanes.

2.10 Mechanically Interlocked Molecules Operating in Aqueous Environments

Stoddart also produced a subset of mechanically interlocked molecules (MIMs), namely donor–acceptor [2]catenanes, (**Figure 22a**) in aqueous solution in good yields from readily available precursors. The catenane formation is templated by strong hydrophobic and [π⋯π] stacking interactions, which together serve to assemble the corresponding supramolecular precursors prior to post-assembly covalent modification

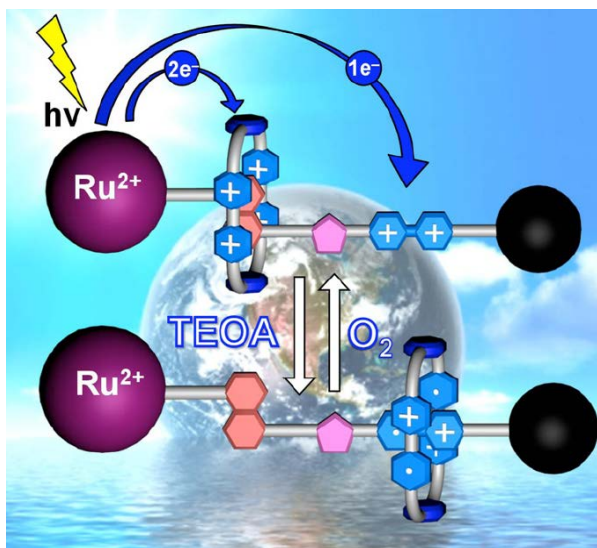


Figure 23. Redox-controllable bistable [2]rotaxane, comprised of (i) a CBPQT⁴⁺ ring component, (ii) a Ru(bpy)₃²⁺ dumbbell component, which serves as one of its two stoppers and also as a photocatalytic unit, (iii) a electron-rich 1,5-dioxynaphthalene (DNP) recognition site for the electron-deficient tetracationic cyclophane, and (iv) a BIPY²⁺ unit, has been designed and synthesized

leading to formation of the mechanical bond. The preparation of mechanically interlocked molecules in water constitutes the basis for the future development of complex functional molecular machinery in aqueous environments. The most sophisticated and efficient nanoscale machines are those which reside in living cells. The rapid development of artificial molecular machinery during the past two decades has rendered it possible to mimic biomolecular machines using wholly synthetic systems — even if the complexity and efficiency of the non-natural counterparts are in no way comparable to their naturally occurring cousins. One of the most important, yet challenging, issues in this field is the development of artificial molecular machinery that can be incorporated into an integrated system while still retaining its capacity to perform molecularly controlled work. Redox-controllable bistable [2]rotaxane (**Figure 23**),

comprised of (i) a CBPQT⁴⁺ ring component, (ii) a Ru(bpy)₃²⁺ dumbbell component, which serves as one of its two stoppers and also as a photocatalytic unit, (iii) an electron-rich 1,5-dioxynaphthalene (DNP) recognition site for the electron-deficient tetracationic cyclophane, and (iv) a BIPY²⁺ unit, has been designed and synthesized. With assistance from the sacrificial electron donor triethanolamine (TEAO), light-triggered switching through numerous cycles can be initiated by radical-pairing interactions between the reduced forms of the CBPQT⁴⁺ ring and the BIPY²⁺ unit of the dumbbell in aqueous solution in the absence of air; the system can be reset by donor-acceptor charge-transfer interactions in the presence of air (O₂). In a manner reminiscent of a machine, the ring can be made to dart back and forth along the axle of the dumbbell from one recognition site to the other (e.g., to the BIPY^{•+} or DNP) in this bistable [2]rotaxane upon exposure to light or molecular oxygen, respectively.

2.11 Solution-Phase Mechanistic Study and Solid-State Structure of a Tris(bipyridinium Radical Cation) Inclusion Complex

Stoddart investigated the ability of the diradical dicationic cyclobis(paraquat-*p*-phenylene) (CBPQT^{2(•+)}) ring to form inclusion complexes with 1,1'-dialkyl-4,4'-bipyridinium radical cationic (BIPY^{•+}) guests (**Figure 24**) both mechanistically and quantitatively. Two BIPY^{•+} radical cations, methyl viologen (MV^{•+}) and a dibutynyl derivative (V^{•+}), were investigated as guests for the CBPQT^{2(•+)} ring.

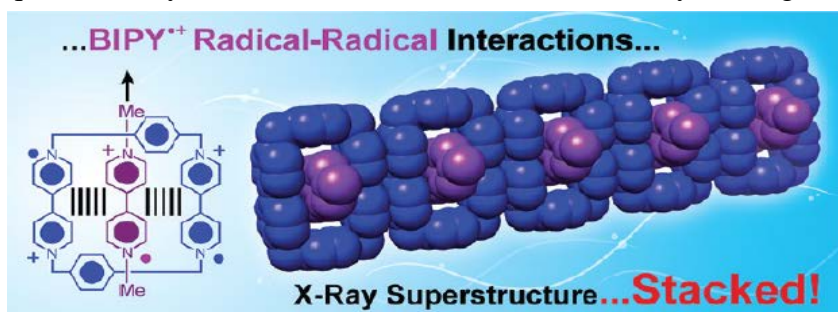


Figure 24. Graphical representation of the light induced switching of a [2]rotaxane in water. Serving the role as both a stopper and electron transfer photocatalyst, the excited state of the Ru²⁺ complex donates a total of two electrons to the ring component and one electron to the dumbbell component, using TEOA to reduce the oxidized Ru³⁺ back to Ru²⁺. Exposure to atmospheric O₂ results in oxidation of the ring and dumbbell components, restoring the initial ground state.

Both guests formed triradical complexes, namely, CBPQT^{2(•+)}⊂MV^{•+} and CBPQT^{2(•+)}⊂V^{•+}, respectively. The structural details of the

CBPQT^{2(•+)}⊂MV^{•+} complex, which were ascertained by single-crystal X-ray crystallography, reveal that MV^{•+} is located inside the cavity of the ring in a

centrosymmetric fashion: the 1:1 complexes pack in continuous radical cation stacks. A similar solid-state packing was observed in the case of CBPQT^{2(•+)} by itself. Quantum mechanical calculations agree well with the superstructure revealed by X-ray crystallography for CBPQT^{2(•+)}⊂MV^{•+} and further suggest an electronic asymmetry in the SOMO caused by radical-pairing interactions. The electronic asymmetry is maintained in solution. The thermo-dynamic stability of the CBPQT^{2(•+)}⊂MV^{•+} complex was probed by both isothermal titration calorimetry (ITC) and UV-vis spectroscopy, leading to

binding constants of $(5.0 \pm 0.6) \times 10^4 \text{ M}^{-1}$ and $(7.9 \pm 5.5) \times 10^4 \text{ M}^{-1}$, respectively. The kinetics of association and dissociation were determined by stopped-flow spectroscopy, yielding a k_f and k_b of $(2.1 \pm 0.3) \times 10^6 \text{ M}^{-1} \text{ s}^{-1}$ and $250 \pm 50 \text{ s}^{-1}$, respectively. The electrochemical mechanistic details were studied by variable scan rate cyclic voltammetry (CV), and the experimental data were compared digitally with simulated data, modeled on the proposed mechanism using the thermodynamic and kinetic parameters obtained from ITC, UV/vis, and stopped-flow spectroscopy. In particular, the electrochemical mechanism of association/dissociation involves a bisradical tetracationic intermediate $\text{CBPQT}^{(2+)(\bullet+)} \subset \text{V}^{\bullet+}$ inclusion complex; in the case of the $\text{V}^{\bullet+}$ guest, the rate of disassociation ($k_b = 10 \pm 2 \text{ s}^{-1}$) was slow enough that it could be detected and quantified by variable scan rate CV. All the experimental observations lead **Stoddart** to the speculation that the $\text{CBPQT}^{(2+)(\bullet+)}$ ring of the bisradical tetracation complex might possess the unique property of being able to recognize both $\text{BIPY}^{\bullet+}$ radical cation and π -electron-rich guests simultaneously. The findings reported herein lay the foundation for future studies where this radical–radical recognition motif is harnessed particularly in the context of mechanically interlocked molecules and increases our fundamental understanding of $\text{BIPY}^{\bullet+}$ radical–radical interactions in solution as well as in the solid state.

2.12 Positive Cooperativity in the Template-Directed Synthesis of Monodisperse Macromolecules

Stoddart synthesized two series of oligorotaxanes **R** and **R'** that contain $-\text{CH}_2\text{NH}_2^+\text{CH}_2-$ recognition sites in their dumbbell components (**Figure 25**) employing

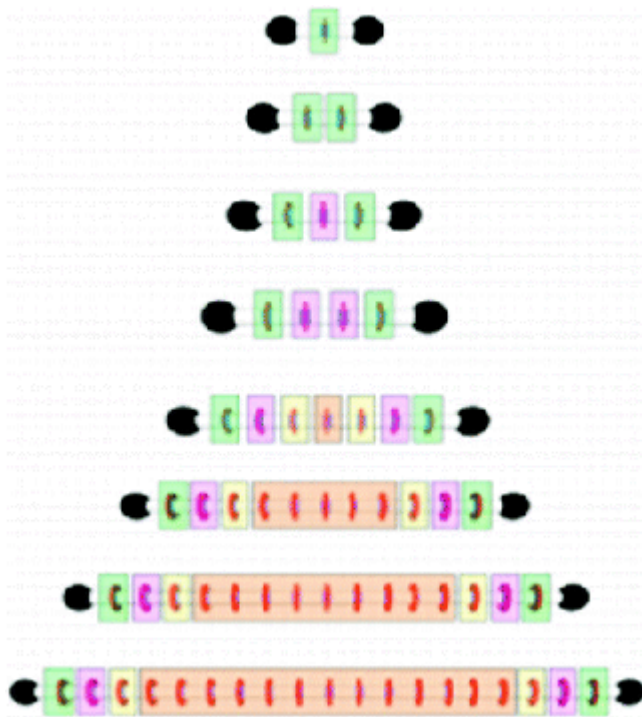


Figure 25. Graphical representation of a series of oligorotaxanes as they increase in size.

template-directed protocols. [24]Crown-8 rings self-assemble by a clipping strategy around each and every recognition site using equimolar amounts of 2,6-pyridinedicarboxaldehyde and tetraethyleneglycol bis-(2-aminophenyl) ether to efficiently provide up to a [20]rotaxane. In the **R** series, the $-\text{NH}_2^+$ recognition sites are separated by trimethylene bridges, whereas in the **R'** series the spacers are *p*-phenylene linkers. The underpinning idea here is that in the former series, the recognition sites are strategically positioned 3.5 Å apart from one another so as to facilitate efficient $[\pi \cdots \pi]$ stacking between the aromatic residues in contiguous rings in the rotaxanes and consequently, a discrete rigid and rod-like conformation is realized; these

noncovalent interactions are absent in the latter series rendering them conformationally flexible/nondiscrete. Although in the R' series, the [3]-, [4]-, [8]-, and [12]rotaxanes were isolated after reaction times of <5–30 min in yields of 72–85%, in the R series, the [3]-, [4]-, [5]-, [8]-, [12]-, [16]-, and [20]rotaxanes were isolated in <5 min to 14 h in 88–98% yields. It follows that while in the R' series the higher order oligorotaxanes are formed in

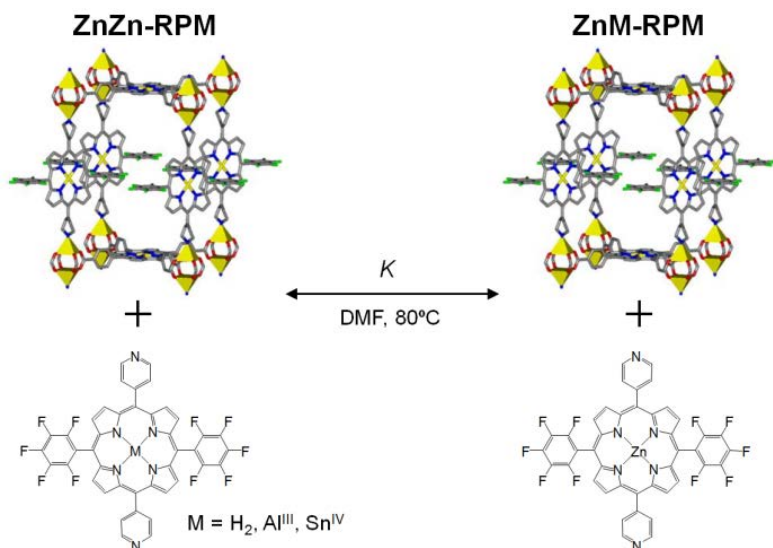


Figure 26. Pillar-based solvent-assisted linker exchange reactions.

lower yields more rapidly, in the R series, the higher order oligorotaxanes are formed in higher yields more slowly. In the R series, the high percentage yields are sustained throughout, despite the fact that up to 39 components are participating in the template-directed self-assembly process. Simple

arithmetic reveals that the conversion efficiency for each imine bond formation peaks at 99.9% in the R series and 99.3% in the R' series. This maintenance of reaction efficiency in the R series can be ascribed to positive cooperativity, that is, when one ring is formed it aids and abets the formation of subsequent rings, presumably because of stabilizing extended $[\pi \cdots \pi]$ stacking interactions between the arene units. Experiments have been performed wherein the dumbbell is starved of the macrocyclic components, and up to five times more of the fully saturated rotaxane is formed than is predicted based on a purely statistical outcome, providing a clear indication that positive cooperativity is operative. Moreover, it would appear that as the R series is traversed from the [3]- to the [4]- to the [5]rotaxane, the cooperativity becomes increasingly positive. **Stoddart** does not observed this cooperative behavior for the analogous oligorotaxanes in the R' series. The conventional bevy of analytical techniques (e.g., HR-MS (ESI) and both ^1H and ^{13}C NMR spectroscopies) help establish the fact that all the oligorotaxanes are pure and monodisperse. Evidence of efficient $[\pi \cdots \pi]$ stacking between contiguous arene units in the rings in the R series is revealed by ^1H NMR spectroscopy. Ion-mobility mass spectrometry performed on the R and R' series yielded the collisional cross sections, confirming the rigidity of the R oligorotaxanes and the flexibility of the R' ones. The extended $[\pi \cdots \pi]$ stacking interactions are found to be present in the solid-state structures of the [3]- and [4]rotaxanes in the R series and also on the basis of molecular mechanics calculations performed on the entire series of oligomers. The collective data presented herein supports **Stoddart's** original design in that the extended $[\pi \cdots \pi]$ stacking between contiguous arene units in the rings of the R series of oligorotaxanes facilitate an essentially rigid rod-like conformation with evidence that positive cooperativity improves

the efficiency of their formation. This situation stands in sharp contrast to the conformationally flexible R' series where the oligorotaxanes form with no cooperativity.

2.13. Metal Organic Framework Materials

The focus of **Hupp's** effort was on supramolecular systems in the form of porous, crystalline metal-organic framework (MOF) materials. The specifics centered on discovering how to synthesize these materials and then rendering these materials competent for chemical catalysis. In many instances the building blocks used to construct functional MOFs resembled active-sites in found in certain metallo-enzymes (e.g. cytochrome oxidases and vitamin B12 cofactors that are metallo-porphyrin based). Among the more significant findings and accomplishments are the following:

- Synthesis of the first carborane-based metal-organic framework material. One of the remarkable features of the carborane MOF is its exceptional thermal stability (i.e. ca. 530K if heated in a nitrogen atmosphere).
- Development of MOF linkers that systematically preclude framework catenation (i.e. templated formation of replica networks within the void spaces of an initially formed MOF structure).
- Demonstration of post-synthetic tailoring of MOF cavities with functional groups capable of capturing metal ions. For the system examined, the desired functional groups (carboxylates) cannot be directly incorporated, as they interfere with the initial synthesis of the MOF.
- Demonstration of spatially selective, post-synthetic chemical tailoring of MOF cavities and surfaces via versatile click chemistry (i.e. copper catalyzed triazole-linkage formation).
- Synthesis of the first metallo-porphyrin based MOF exhibiting both molecular porosity and catalytic activity. Nearly 60 previous reports describing unsuccessful attempts had been published before our work appeared.
- Development of a more general synthesis route to robust, porous and potentially catalytically active, porphyrinic MOFs (termed RPMs), including MOFs featuring complementary pairs of porphyrins containing differing metal centers.
- Demonstration of carbene-like catalytic activity based on high-stability zeolitic imidazolate frameworks (ZIFs).
- Demonstration of multi-site, hydrogen-bond-based catalysis within a new MOF material. The material is competent for catalysis because the comparatively rigid architecture of prevents activating moieties from engaging in unproductive self-recognition – a substantial problem with analogous solution-phase catalysts, especially when deployed in low polarity solvent environments.

Below are more in-depth descriptions of two advances achieved by **Hupp** in collaboration with **Mirkin**, **Nguyen**, **Ratner**, and **Stoddart**. Both are based on the newly developed concept of solvent-assisted linker exchange (SALE) and both have been used to obtain catalytically active MOFs that appear to be impossible to obtain by *de novo* synthesis methods.

Solvent-assisted linker exchange has been shown to be a useful strategy for introducing free-base porphyrins and new metallo-porphyrins into robust porphyrinic metal-organic framework (RPM) materials, where the exchanging linkers are dipyridyl-porphyrin pillars (**Figures 26 and 27**). Depending on RPM crystallite size, SALE equilibrium is achievable within one to several days – with smaller crystallites equilibrating more rapidly. The exchange process is spatially anisotropic, occurring via channels directed along the *a* or *b* axes, but not via the small channels directed along the *c* axis. **Hupp** found that linker exchange can be driven to completion (or nearly so) by repetitively introducing exchangeable linkers. Among the new materials that can be prepared via SALE are ZnAl-RPM, ZnSn-RPM, ZnH₂-RPM, ZnCo-RPM-(cobalt node), and Zn₂H-RPM-(nickel node). The first of these was found to be competent as a catalyst for epoxide ring-opening by trimethylsilylazide. The last two were accessed via linker-metallation and/or node-metal-exchange, starting from SALE-prepared Zn₂H-RPM. Notably, most, if not all, of the new RPMs are difficult, or perhaps impossible, to prepare via direct solvothermal methods, underscoring the utility of SALE. More generally, SALE shows considerable promise as a strategy for

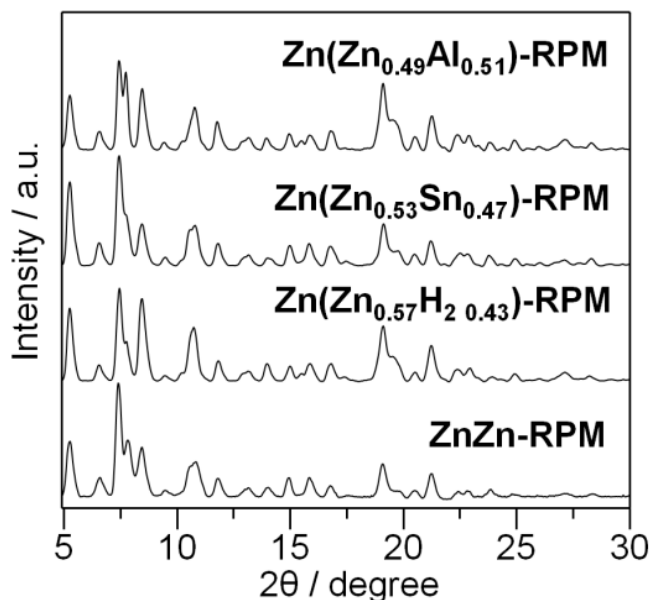


Figure 27. PXRD patterns of partly linker-exchanged samples together with that of Zn-Zn-RPM.

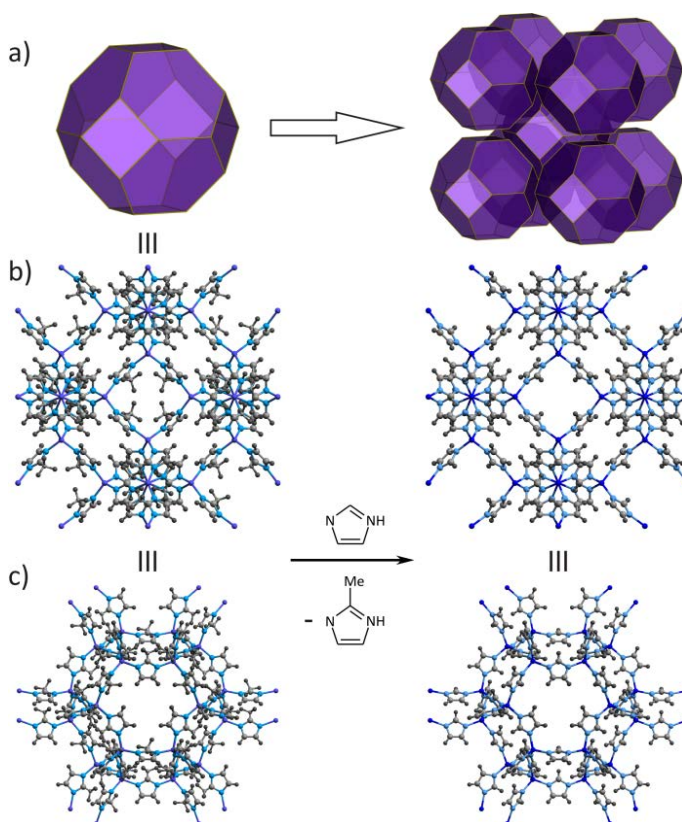


Figure 28. (a) 3D representation of the tiling of the SOD topology. (b) View along the crystallographic *a* axis, (c) view along [111] direction of ZIF-8 (left) and SALEM-2 (right).

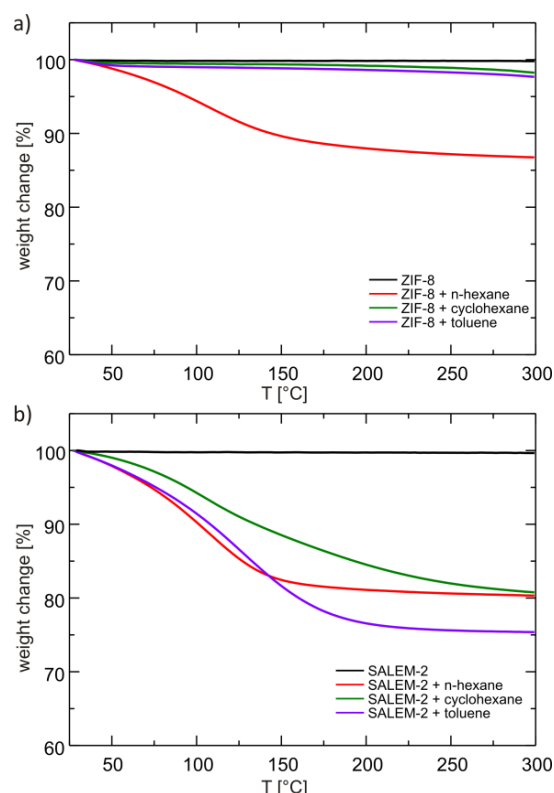


Figure 29. (a) ZIF-8 releases – and therefore is initially permeated by – only *n*-hexane (kinetic diameter 4.3 Å). (b) SALEM-2 accommodates *n*-hexane, but also takes up and releases both cyclohexane (kinetic diameter 6.0 Å) and toluene (kinetic diameter 6.1 Å).

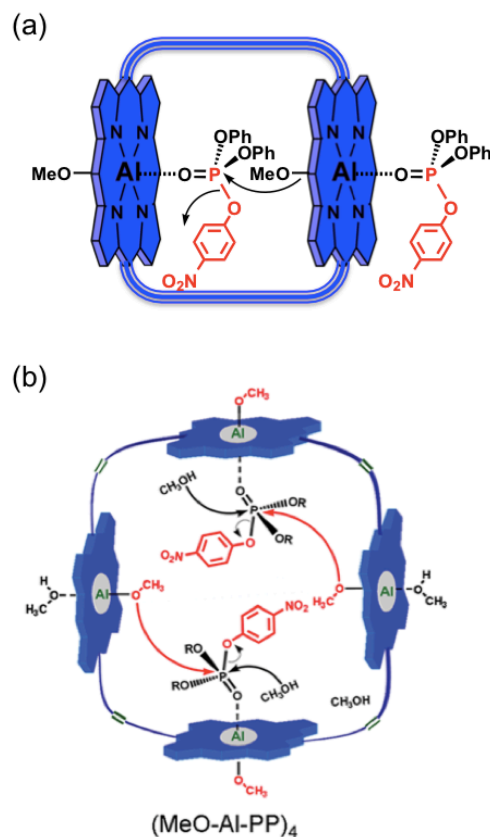


Figure 30. Proposed catalytic methanolysis of a phosphate triester in an Al porphyrin dimer (a) and tetramer (b).

synthesizing otherwise inaccessible metal-organic framework materials.

Hupp also synthesized a remarkably open and interior-accessible zeolitic imidazolate framework (ZIF) material of sod topology, possessing unsubstituted imidazolate linkers, via solvent-assisted linker exchange (SALE) (**Figures 28 and 29**). The new material is a long sought analogue of the archetypal material, ZIF-8. Indeed, earlier work from several labs had yielded seventeen “wrong” polymorphs of the desired new material, where each of the polymorphs lacked several of the following features: substantial void volume, substantial internal surface area, flexible apertures, synthetic scalability, and catalytic activity. Computational work from other labs had previously established that the desired polymorph was inherently less stable thermodynamically than any of the readily synthetically accessible polymorphs. The structure of the new material, SALEM-2, has been confirmed through ¹H NMR spectroscopy, and powder and single-crystal X-ray diffraction studies. SALEM-2 is the first example of a porous Zn(imidazolate)₂ ZIF possessing a truly zeolitic topology that can be obtained in bulk quantities. Upon treatment with *n*-butyl lithium, the open analogue exhibits Brønsted base catalysis that cannot be accomplished by the parent material ZIF-8. SALE appears to be a powerful technique that allows the incorporation of structurally and chemically attractive ligands into ZIFs that cannot be obtained *de novo*.

2.14 Supramolecular porphyrin assemblies for the remediation of chemical warfare agents

Given their utility in molecular recognition, chemical catalysts, light-harvesting and energy conversion, and chemical sensing, **Nguyen** and **Hupp's** work has focused on the use of metallo-porphyrins and conjugated organic molecules as building blocks for supramolecular assemblies, MOFs, and POPs. The **Nguyen** and **Hupp** groups have developed the facile preparation of covalently linked hollow metalloporphyrin assemblies via templated ring-closing metathesis (tRCM). This versatile strategy can serve as a general route to a multitude of synthetic multiporphyrin hosts with tunable cavity size from a single modular building block (**Figure 30**). Furthermore, because the tRCM linkage chemistry is compatible with a wide range of porphyrin modification chemistries, such synthetic hosts can readily be tuned to engender supramolecular recognition capabilities and enzyme-like catalysis activities that are not expressed in single-porphyrin systems. Recently, a (porphyrin)Al^{III} tetramer has been demonstrated to be a highly active catalyst for the methanolysis of *p*-nitrophenyl diphenyl phosphate (PNPDPP, a simulant for nerve agent). In the presence of 3 mol% (MeO-Al-PP)₄, a rate acceleration of 430 over the uncatalyzed reaction was observed in a mixture of MeOH and CHCl₃ (1:1 v/v) (**Figure 31**).

Interestingly, **Nguyen** and **Hupp** observe a difference in binding stoichiometry between the organophosphate substrate and supramolecular assemblies, with the larger tetrameric (porphyrin)Al^{III} catalyst accommodating two substrates and the smaller

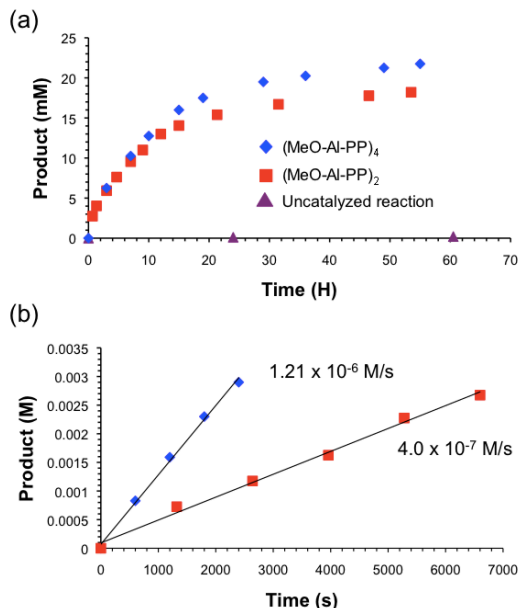


Figure 31. (a) Reaction profile for the methanolysis of PNPDPP and (b) initial reaction rates for (porphyrin)Al^{III} tetramer and dimer catalysts

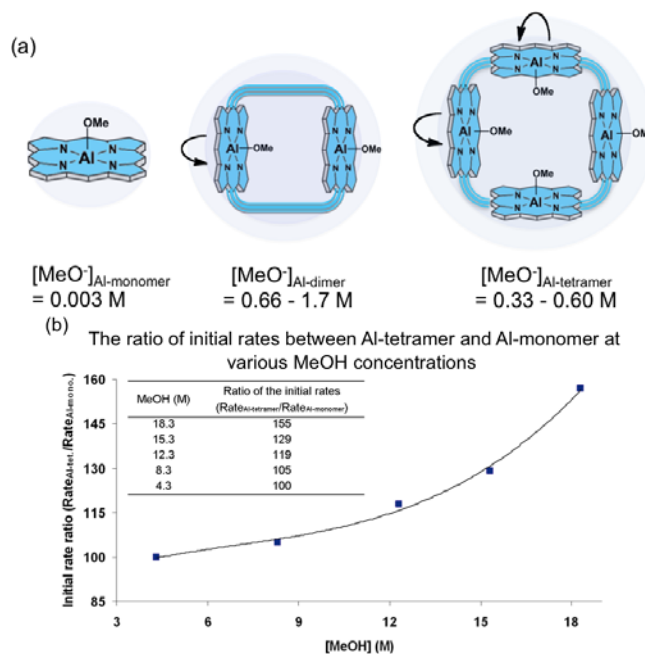


Figure 32. (a) Local concentration of methoxide in supramolecular porphyrin assemblies and (b) the ratio of product formation rates between (MeO-Al-PP)₄ and MeO-Al-PP at various methanol concentrations.

dimeric species accommodating one. This difference in binding stoichiometry is reflected in the catalytic activity, as a dimeric (porphyrin)Al^{III} catalyst is able to bind one PNPDP substrate in a smaller volume, leading to a higher reactant concentration and an enhanced catalytic rate. Under the same conditions, (MeO-Al-PP)₂ displayed a rate acceleration of 3 over (MeO-Al-PP)₄, and more than 1300 over the uncatalyzed reaction. Mechanistic studies underlined the importance of having a high local concentration of methoxide ion that operates in concert with methoxide ligand in the vicinity of monomeric, dimeric, and tetrameric (porphyrin)Al^{III} species, up to a 550 fold increase in methoxide concentration is observed over the monomer species (**Figure 32**), further illustrating the importance of high local methoxide concentration. Additionally, increasing the methanol concentration leads to an increase in the ratio of initial rates between (MeO-Al-PP)₄ tetramer and MeO-Al-PP monomer (**Figure 32**), as more polar solvent conditions solvophobically drive the PNPDP substrate into the cavity.

2.15 Encapsulation of fullerene in supramolecular porphyrin dimers and tetramers

Nguyen and Hupp also showed that fullerene could be encapsulated in supramolecular porphyrin-containing complexes. The solvophobically driven encapsulation of substrates inside the cavity can be illustrated by the ability of

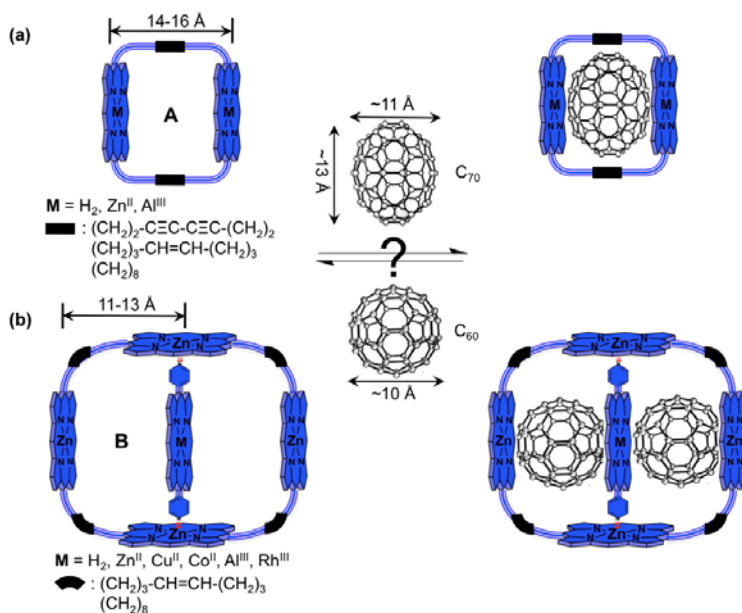


Figure 33. Schematic representation of selective fullerene binding by co-facial porphyrin dimers possessing linkers with tunable rigidity and bisected Zn(porphyrin) tetramers.

(porphyrin)Al^{III} tetramer and dimer to bind fullerene and its derivatives. These assemblies are good candidates for fullerene encapsulation due to their rigidity, tunable cavity sizes, and strong pi-pi interactions with guest molecules. In toluene, (MeO-Al-PP)₂ can bind 1 equivalent of C₆₀ or C₇₀ to produce a 1:1 fullerene inclusion complex with an association constant of 2.6×10^6 and 1.1×10^7 M⁻¹, respectively (**Figure 33**). Interestingly, for the 1:1 complexation of C₆₀ with a (porphyrin)M-templated (porphyrin)Zn tetramer (Figure 4b, M = H₂, Zn, Cu, Co, Al-OMe, Rh-Me), the

association constant is only $\sim 10^4$ M⁻¹ for a 1:1 complex, regardless of the identity of the (porphyrin)M template. Molecular modeling suggested that the 1:1 binding stoichiometry and the smaller affinity of this (porphyrin)M-templated Zn tetramer for fullerene (compared to that for the dimer) can be attributed to the very tight fitting of the first bound fullerene. Indeed, hydrogenation of the four double bonds on the periphery of the

(porphyrin)Zn tetramer, followed by templation with (porphyrin)Al^{III} allows the resulting assembly to have an increased binding constant of $1.5 \times 10^5 \text{ M}^{-1}$, indicating the importance of a flexible cavity towards stabilization of C₆₀.

2.16 Robust porphyrinic materials for the degradation of chemical warfare agents

Analogous to the catalytic methanolysis of phosphate esters using supramolecular porphyrin assemblies (*vide supra*) degradation of phosphate esters can be accomplished using robust porphyrinic materials (RPMs) (**Figure 34**).

The synthetic approach of RPMs by **Nguyen** and **Hupp** employed a space-filling

tetracarboxylated porphyrin ligand in concert with a bulky dipyrindyl porphyrin pillar, which

generated a zinc metal node pillared paddlewheel motif. Not only does the zinc and aluminum-based RPM exhibit enhanced rates for the methanolysis of phosphate esters in comparison to their aluminum porphyrin supramolecular counterparts, RPMs also have the potential for the highly desired hydrolysis of phosphate esters as the well-defined, crystalline, highly porous materials are robust and stable towards a variety of reaction conditions including hydrolysis.

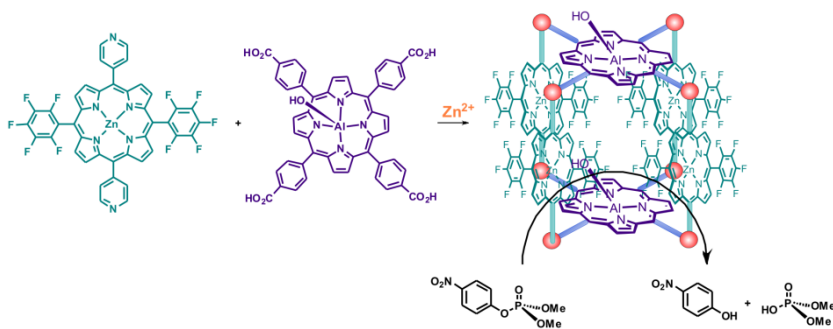


Figure 34. Synthesis of a catalytically active RPM for the hydrolysis of phosphonate esters.

2.17 Tuning MOF hydrophobicity for selective adsorption

A series of six isostructural zinc-based paddlewheel MOFs were synthesized by **Nguyen** and **Hupp** utilizing a space-filling dibromo tetratopic carboxylate ligand, which prohibits catenation, and dipyrindyl ligands bearing alkyl chains of various lengths (methyl, ethyl, propyl, butyl,

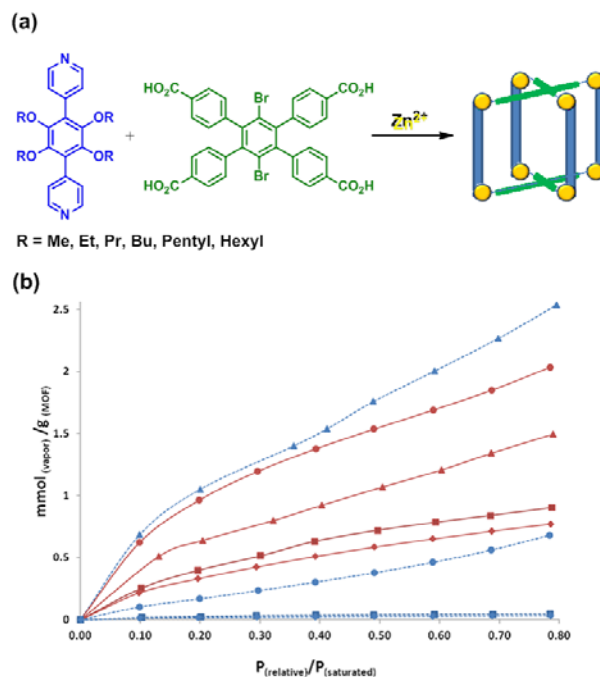


Figure 35. (a) Synthesis of MOFs with various alkyl chain lengths. (b) Vapor isotherms at 25 °C for methyl substituted MOF (blue dotted line) and hexyl substituted MOF (red solid line) (triangle = water, circle = ethanol, square = toluene, and diamond = pentane).

pentyl, or hexyl), which engenders varied degrees of hydrophobicity (**Figure 35**). This series of MOFs exhibits high stability to water, unlike many current MOFs. Moreover, the degree of hydrophobicity can be tuned depending on the length of the installed alkyl chain allowing for selective adsorption. **Figure 35** illustrates how the methyl bearing MOF selectively adsorbs water over ethanol while the adsorption of pentane and toluene is negligible; on the other hand, the hexyl substituted MOF selectively adsorbs ethanol over water with reasonable adsorption of the larger non-polar pentane and toluene vapors. The tunable nature of these MOFs and their selective adsorption properties suggests potential for uses in separations.

2.18 First-Principles based Computational Modeling of Catalytic Metal-Organic Frameworks with Focus on Selective Reactant Binding and Reactant Preconcentration

MOFs are crystalline, porous materials comprised of an organic backbone anchored by metal ions, metal complexes or metal-ion clusters. The structure and functionality of the organic ligands and the metal species, termed 'secondary building blocks', determine the dimensions of the pores as well as the reactivity of the MOF. By choosing suitable components, the chemical environment and pore size of a MOF can be designed to target specific molecules. While the organic components of MOFs compromise their stability at high temperatures, they create innumerable possibilities for structures with tailored properties.

Catalytic MOFs have captured widespread attention for displaying shape, size, chemical, and enantiomeric selectivity characteristic of biological enzymes. The vast chemical space available for the design of MOF-based catalysts presents an exciting opportunity for theoretical modeling to guide the development of materials with specific reactivities. The research groups of **Hupp** and **Nguyen** synthesized a stable, crystalline, microporous, zinc-porphyrin-based metal organic framework (ZnPO-MOF) that incorporates the catalytic activity of metalloporphyrins (**Figure 36**). They observed a 236-fold initial acceleration of a prototypical acyl-transfer reaction (**Figure 37**) between 3-pyridylcarbinol (3-PC) and N-acetylimidazole (NAI) by ZnPO-MOF, and attributed this catalysis primarily to a high local concentration or 'preconcentration' of reactants at the porphyrin-Zn active sites of the framework. Isomers of 3-PC underwent similar rate acceleration.

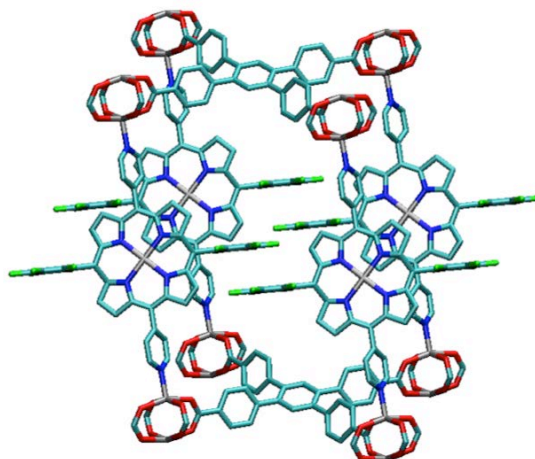


Figure 36. Structure of ZnPO-MOF synthesized by Hupp and Nguyen groups.

Ratner developed an efficient, first-principles-based theoretical model to study active-site reactant preconcentration in catalytic MOFs, and tested it on the acyl-transfer reaction studied by **Hupp** and **Nguyen**. The model has three components: (a) Electronic structure calculations of reactant binding at the active site of the MOF using Density Functional Theory (DFT), (b) Calculation of temperature-dependent binding constants using concepts of standard statistical thermodynamics and DFT results, and (c) Calculation of preconcentration-induced catalytic rate enhancement using calculated binding constants and a proposed

kinetic model that clearly distinguishes between heterogeneous and homogeneous catalysis. Each step of the model independently provides valuable chemical insight into reactant binding and product removal inside the MOF. Cumulatively, the model calculates the preconcentration-derived rate enhancement in order to quantitatively evaluate the importance of preconcentration. Results reproduce important experimental results, and show that reactants bind to the densely packed porphyrin-Zn active sites of the ZnPO-MOF, resulting in a high local concentration of catalyst-bound reactant.

The model predicts that reactant preconcentration in ZnPO-MOF can increase the initial rate of the acyl-transfer reaction by about two orders of magnitude relative to the uncatalyzed reaction, and strongly suggests that it is the dominant catalytic mechanism in this particular system. An important conclusion of the theoretical study is that preconcentration can be exploited as an independent means to enhance MOF catalysis. It can augment catalysis due to transition-state stabilization. The model is not limited to this particular MOF, but rather can be applied as a computational tool to examine the importance of preconcentration, the temperature dependence of preconcentration, and product inhibition for a given reaction in a given catalytic MOF. It can also be used in the design of catalytic MOFs with optimum preconcentration properties, and in the design of MOFs with optimum sensing properties towards specific target molecules.

The three-step theoretical model and some key results are described here. In the first step, DFT calculations were performed on the full atomistic structure of ZnPO-MOF using the Vienna *ab initio* simulation package (VASP, version 4.6.36), a code that uses plane waves as the basis set. VASP imposes periodic boundary conditions on a given unit cell to model an infinite crystal, and is therefore ideal for studying ground-state properties of crystalline solids. The unit cell of ZnPO-MOF has dimensions, $a = 11.569 \text{ \AA}$, $b = 15.447 \text{ \AA}$, $c = 21.190 \text{ \AA}$, $\alpha = 76.79^\circ$, $\beta = 79.03^\circ$, and $\gamma = 89.61^\circ$. It consists of 137 atoms, including 3 Zn atoms, 10 F atoms, 8 O atoms, 6 N atoms, 76 C atoms, and 34 H atoms.

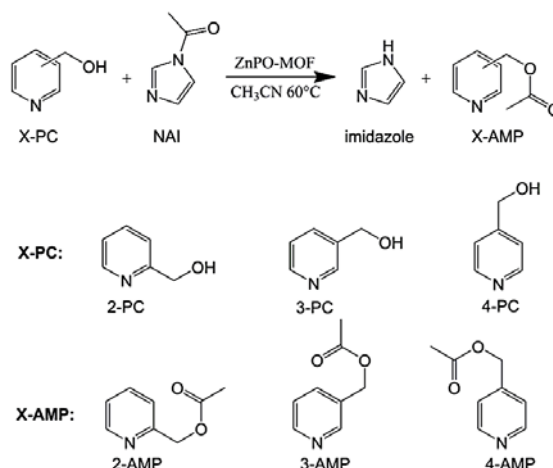


Figure 37. Acyl transfer reaction between isomers of pyridylcarbinol (PC) and N-acetylimidazole (NAI).

The physical quantities calculated using DFT were the binding energies, binding geometries, and vibrational frequencies of reactant, product, and solvent molecules bound to the catalytic porphyrin-Zn sites of the MOF. **Figure 38** shows the final optimized geometries of 3-PC (**Figure 38a**) and NAI (**Figure 38b**) bound to the porphyrin-Zn active site of ZnPO-MOF. The calculated binding energies of NAI, 3-PC and its isomers, 2-PC and 4-PC, fall in the range of 9-14 kcal/mol, with 2-PC binding the least strongly due to steric repulsion. All reactants bind more strongly than solvent, demonstrating that reactants can displace solvent molecules from the MOF porphyrin-Zn sites and preconcentrate at the MOF active sites. Product binding is similar to that of reactants, suggesting that product molecules, in particular imidazole and 3-AMP, can block

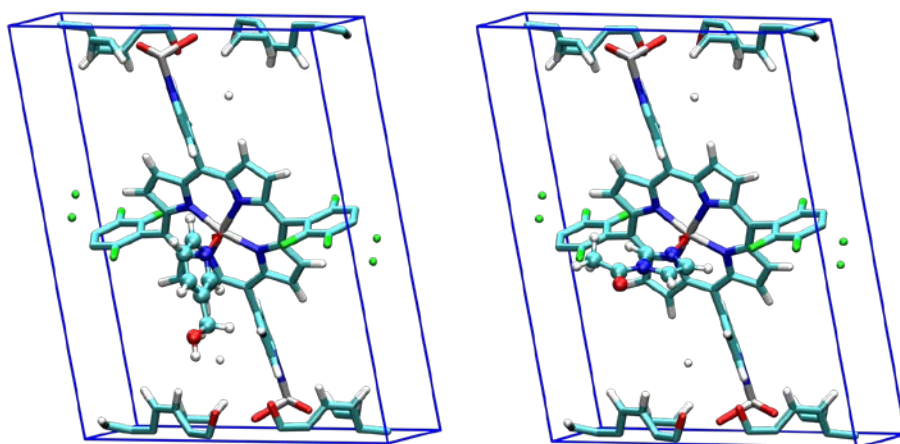


Figure 38. DFT-optimized geometries of reactants, (a) 3-pyridylcarbinol (3-PC) and (b) N-acetylimidazole (NAI), bound to the catalytic porphyrin-Zn sites of ZnPO-MOF.

catalytic sites at high concentrations. The high binding energy of imidazole corroborates the experimental results of **Hupp** and **Nguyen** that demonstrate formidable product inhibition by imidazole.

The second step of the theoretical model utilizes the results of the DFT study to calculate temperature-dependent equilibrium constants for reactant binding and product dissociation. The equilibrium describing the displacement of bound solvent molecules from the MOF active sites by reactant molecules is defined as,

$$K(T) = \frac{[\text{MOF-reactant}]}{[\text{MOF-solvent}][\text{reactant}]} = \frac{Q_{\text{MOF-reactant}} Q_{\text{solvent}}}{Q_{\text{MOF-solvent}} Q_{\text{reactant}}}$$

where $K(T)$ is the temperature-dependent equilibrium constant, $[\text{MOF-reactant}]$ is the concentration of reactant-bound porphyrin-Zn sites in the MOF, $[\text{MOF-solvent}]$ is the concentration of solvent-bound porphyrin-Zn sites in the MOF, and $[\text{reactant}]$ is the concentration of reactant in solution. Since the concentration of solvent can be assumed to be constant, it is set equal to 1 in accordance with concepts of heterogeneous equilibria. Therefore, it does not appear in the numerator of the first quotient. The four Q 's are the canonical partition functions for the respective species. These partition functions can be calculated using concepts of standard statistical thermodynamics, known physical constants, and the DFT results from the previous step. Dissociation of products from the MOF active sites can be described similarly, using a product-solvent

equilibrium instead of a reactant-solvent equilibrium. Results show that 3-PC has the highest binding constant of 1906 M⁻¹ at 60°C, whereas 2-PC has the lowest binding constant of 0.2 M⁻¹ at 60°C due to steric repulsion. These values show that NAI, 3-PC and 4-PC will effectively preconcentrate at the active sites of the MOF. Imidazole has a low dissociation constant and consequently will be difficult to remove from the MOF active sites. Once again, this result agrees with the product inhibition by imidazole observed by **Hupp** and **Nguyen**.

The final step determines the preconcentration-based catalytic rate enhancement due to heterogeneous catalysis by the MOF. The total rate enhancement is defined as:

$$\frac{\text{Rate}_{\text{cat-hetero}}}{\text{Rate}_{\text{uncat}}} = \left(\frac{k_r'}{k_r} \right) \left\{ \frac{\theta_{R1} [R2]_0 + \theta_{R2} [R1]_0}{[R1]_0 [R2]_0} \right\} [\text{Porphyrin}_{\text{MOF}}]_0,$$

where

$$\theta_{R1} = \frac{K_{b1}}{1 + K_{b1} + K_{b2}},$$

and

$$\theta_{R2} = \frac{K_{b2}}{1 + K_{b1} + K_{b2}}.$$

In the above equations, k_r and k_r' denote the rate constants of the MOF-catalyzed and uncatalyzed reactions, respectively, $[R1]_0$ and $[R2]_0$ denote the initial reactant concentrations, θ_{R1} and θ_{R2} denote the reactant-bound fractions of the total metalloporphyrin concentration inside the MOF, $[\text{Porphyrin}_{\text{MOF}}]_0$, and K_{b1} and K_{b2} denote the binding constants of the reactants. To calculate the preconcentration-induced enhancement, it was assumed that $k_r = k_r'$, *i.e.*, there was no transition-state stabilization and catalysis was solely due to preconcentration. The initial reactant concentrations of $[\text{NAI}]_0 = 6$ mM and $[\text{PC}]_0 = 9$ mM, and a reaction temperature of 60 °C were used in accordance with **Hupp** and **Nguyen's** experiments. The solvent-accessible void volume of the ZnPO-MOF unit cell, as calculated by **Hupp** and **Nguyen** using the SQUEEZE program is 2069.6 Å³. Since there is one porphyrin per unit cell, the concentration of porphyrins in the MOF = $[\text{Porphyrin}_{\text{MOF}}]_0 = 0.802$ M. The reactant binding constants, K_{b1} and K_{b2} , were determined in the previous step of the model. Results show that reactant preconcentration can increase the initial catalytic rate enhancement by factors of 92 for NAI+3-PC, 133 for NAI+2-PC, and 118 for NAI+4-PC. A comparison of the experimentally observed enhancement factor of 236 for 3-PC to the calculated preconcentration-based enhancement factor of 92 strongly suggests that preconcentration is the major component of the total rate enhancement in this system. In addition, the calculated enhancement factor is similar for all three isomers, just as the observed total rate enhancement is also similar for all three isomers. This agreement further indicates that preconcentration is the dominant catalytic mechanism in this system, since activation energies and collision frequencies would be more sensitive to structural variations in isomers.

To summarize, the theoretical study performed by **Ratner** demonstrates that reactant preconcentration in MOFs can enhance catalysis by two orders of magnitude. The theoretical model of MOF catalysis proposed by the group can be used to examine active-site preconcentration in different MOFs and to design catalytic MOFs with optimal preconcentration properties. Here are some specific applications of the model:

1. The model can be used to calculate binding constants of reactants and dissociation constants of products at the active site of a MOF. The binding constants will reveal how effectively the reactants will preconcentrate, and which reactants will preconcentrate more. The dissociation constants will reveal which products will cause serious inhibition of catalysis as product concentrations increase. If the active-site environment of the MOF or the shape and size of MOF channels is unfavorable for the reactants under consideration, our periodic model will capture the problem in the form of low binding energies and binding constants. This method for calculating molecular binding constants can also be applied in the design of MOFs that sense small target molecules.
2. The model can be used to study the temperature dependence of binding and dissociation constants of reactants and products, respectively, in order to choose optimum temperatures for the catalytic reaction. Low temperatures can help to increase reactant preconcentration while high temperatures can help curb product inhibition.
3. The kinetic analysis can be used to predict the maximum initial rate enhancement possible from preconcentration in a given MOF structure with known initial reactant concentrations and calculated active-site reactant binding constants. Consequently, this model can help to tune these parameters in order to optimize reactant preconcentration. In addition, this model can aid in the design of MOF architectures that maximize the concentration of active sites without sterically hindering reactant binding.

2.19 Monte-Carlo Analysis of Solvent Effects in Catalytically Active Metal-Organic Frameworks

While a molecular-level study of catalysis by ZnPO-MOF catalysis addresses the microscopic binding properties of reactants, products and solvent, it is unable to address important macroscopic effects such as solvent packing and reactant diffusion because it models ZnPO-MOF in vacuum. In order to understand the flow of reactants to the catalytic sites of solvent-filled ZnPO-MOF, Monte Carlo simulations were performed by **Ratner** using the Monte Carlo for Complex Chemical Systems Towhee (MCCCS Towhee) package. The MOF structure was modeled as a rigid structure with coordinates and charges determined from DFT calculations. The solvent and reactants were grown using Configurational-bias Monte Carlo (CBMC) with charges assigned from DFT. The interactions of the solvent and reactants with ZnPO-MOF were described using the OPLS and DREIDING force fields.

Using the chemical potential values calculated by Towhee, Grand-Canonical Monte Carlo (GCMC) simulations were implemented to fill ZnPO-MOF with solvent. Thermogravimetric analysis provided by studies of **Hupp** and **Nguyen** showed accumulation of 45% solvent by weight of dimethylformamide (DMF) inside the ZnPO-MOF, which corresponds to 61 DMF molecules inside the MOF simulation cell. The GCMC simulation fills the MOF with ~65 DMF molecules, showing excellent agreement

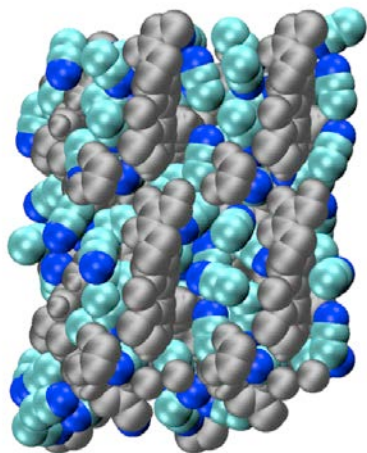


Figure 39. Results of Monte-Carlo simulations showing crowding of acetonitrile (blue and cyan) solvent molecules inside ZnPO-MOF (grey).

between simulation and experiment.

With acetonitrile, the solvent used in the acyl-transfer reaction between 3-pyridylcarbinol and N-acetylimidazole described in the previous section, the simulations find ~96 CH_3CN molecules inside the MOF structure. This amount of solvent leads to a highly congested system, restricting movement to frustrated rotations. It is apparent that any significant movement by either reactant or solvent in this system will be exceeding slow, much longer than any feasible

molecular dynamics simulation can capture. This result also matches well with the slow absolute acyl-transfer rates observed in experiments by **Hupp** and **Nguyen**. Overall, the study indicates that the approach of reactants to the catalytic sites, expected to be the rate-determining step of the reaction is controlled by diffusion. **Figure 39** shows the crowding of acetonitrile solvent inside ZnPO-MOF.

3. PEOPLE (2007-2012)

Faculty

Yuri Berlin (Research Professor)
 Omar Farha (Research Professor)
 Vladimiro Mujica (Research Professor)
 Sarah Hurst (Research Professor)
 Joe Hupp
 SonBinh Nguyen
 Chad Mirkin
 J. Fraser Stoddart
 Mark Ratner

Staff

Sabine Sturm (Mirkin)
 Sarah Kalmon (Mirkin)
 Pamela Watson (Mirkin)

Postdocs

Hyojong Yoo (Mirkin)
Hyung Eui Lee (Hupp)
Omar Farha (Hupp)
Jeongyong Lee (Hupp)
Suk Joong Lee (Hupp/Nguyen)
Kyoung-Tae Youm (Hupp/Nguyen)
Eui-Hyun Ryu (Nguyen)
Chad Risko (Ratner)
Joseph Lakovits (Ratner)
Thorsten Hansen (Ratner)
Jeongyong Lee (Scheidt)
Ignacio Franco (Ratner)
Subhadeep Basu (Stoddart)
Forian Beuerle (Stoddart)
Ali Cockun (Stoddart)
Jungseok Heo (Mirkin)
Dongwoo Kim (Mirkin)
Ignacio Franco (Ratner)
Cheon Yeon Lee (Hupp)
Florian Beuerle (Stoddart)
Mitchell Weston (Nguyen)
Debashis Adhikari (Nguyen)
Tiffany Halo (Mirkin)
Jung Su Park (Mirkin)
Jeremiah Gassensmith
Karel Hartlieb (Stoddart)
Cory Valente (Stoddart)
Sharani Roy (Ratner)
Robert Kennedy (Mirkin)
Ho-Jin Son (Hupp)
Nak Cheong Jeong (Hupp)
Chang Yeon Lee (Hupp/Nguyen)

Graduate Students

Hyo-Jae Yoon (Mirkin)
Jonathan Cave (Mirkin)
Mary Faia (Hupp)
Bradley Hauser (Hupp)
Rebecca Jensen (Hupp)
Tina Li (Hupp)
Karen Mulfort (Hupp)
Michael Devries (Hupp)
Abraham Shultz (Nguyen)
Tendai Gadzikwa (Nguyen)

Justine Shaw (Ratner)
John Roberts (Scheidt)
Dustin Hawker (Scheidt)
Lei Fang (Stoddart)
Doug Friedman (Stoddart)
Travis Gasa (Stoddart)
Mark Olsen (Stoddart)
Kaushik Patel (Stoddart)
Alex Shveyd (Stoddart)
Ryan Totten (Nguyen)
Byungman Kang (Nguyen)
Sonia Ortiz (Nguyen)
Amelia Delaquil (Nguyen)
Justine Shaw-Condo (Ratner)
John Roberts (Scheidt)
Gokham Barin (Stoddart)
Marianne Lalonde (Scheidt)
Alexander Spokoyny (Mirkin)
Michael Wiester (Mirkin)
Charles Machan (Mirkin)
Daniel Clingerman (Mirkin)
Jonathan Barnes (Stoddart)
Ashish Basuray (Stoddart)
Olga Karagiari (Hupp)
Mari Rosen (Mirkin)
Alejo Lifschitz (Mirkin)
Christopher McGuirk (Mirkin)
Jose Mendez (Mirkin)
Josh Cutler (Mirkin)
Mark Langille (Mirkin)
Maria Cabezas (Mirkin)
Alyssa Chinen (Mirkin)
Carson Bruns (Stoddart)
Hao Li (Stoddart)
Henry Heitzer (Ratner)
Chris George (Ratner)

Undergraduate Students

Bi-Shun Zeng (Nguyen)

4. PUBLICATIONS (2007-2012)

1. Berlin, A.; Risko, C.; Ratner, M. A. "Geometric and Chelation Influences on the Electronic Structure and Optical Properties of Tetra(carboxylic acid)phenyleneethynylene Dyes," *J. Phys Chem A* **2008**, *112*, 4202-4208.
2. Banholzer, M. J.; Millstone, J. E.; Mirkin, C. A. "Rationally Designed Nanostructures for Surface Enhanced Raman Spectroscopy," *Chemical Society Reviews* **2008**, *37*, 885-897.
3. Chan, A.; Scheidt, K. A. "Highly Stereoselective Formal [3+3] Cycloaddition of Enals and Azomethine Imines Catalyzed by *N*-Heterocyclic Carbenes," *J. Am. Chem. Soc.* **2007**, *129*, 5334-5335.
4. Chan, A. and Scheidt, K. A. "Direct Amination of Homoenolates Catalyzed by *N*-Heterocyclic Carbenes," *J. Am. Chem. Soc.* **2008**, *130*, 2740-2741.
5. Custar, D. W.; Zabawa, T. P.; Scheidt, K. A. "Total Synthesis and Structural Revision of the Marine Macrolide Neopeltolide," *J. Am. Chem. Soc.* **2008**, *130*, 804-805.
6. Dieringer, J. A.; Lettan, R. B., II; Scheidt, K. A.; Van Duyne, R. P. "Isotope Labeled Single Molecule Surface-Enhanced Raman Spectroscopy: Existence Proof and Dynamics" *J. Am. Chem. Soc.* **2007**, *129*, 16249-16256.
7. Farha, O. K.; Spokoyny, A. M.; Mulfort, K. L.; Hawthorne, M. F.; Mirkin, C. A.; Hupp, J. T. "Synthesis and Hydrogen Sorption Properties of Carborane-Based Metal-Organic Framework Materials," *J. Am. Chem. Soc.* **2007**, *129*, 12680-12681.
8. Galliford, C. V.; Scheidt, K. A. "Pyrrolidinyl-Spirooxindole Natural Products as Inspirations for the Development of Therapeutic Agents," *Angew. Chem. Int. Ed.* **2007**, *48*, 2436-2445.
9. Gibbs-Davis, J. M.; Hayes, P. L.; Scheidt, K. A.; Geiger, F. M. "Anion Chelation by Amino Acid-Functionalized Fused Quartz/Water Interfaces Studied by Nonlinear Optics," *J. Am. Chem. Soc.* **2007**, *129*, 7175-7184.
10. Heo, J.; Jeon, Y.-M.; Mirkin, C. A. "Reversible Interconversion of Homochiral Triangular Macrocycles and Helical Coordination Polymers," *J. Am. Chem. Soc.* **2007**, *129*, 7712-7713.
11. Kuwabara, J.; Stern, C. L.; Mirkin, C. A. "A Coordination Chemistry Approach to a Multieffector Enzyme Mimic," *J. Am. Chem. Soc.* **2007**, *129*, 10074-10075.
12. Kuwabara, J.; Ovchinnikov, M. V.; Stern, C. L.; Mirkin, C. A. "The Reactivity of Dinuclear Rhodium(I) Macrocycles Formed via the Weak-Link Approach," *Organometallics* **2008**, *27*, 789-792.
13. Lee, J.-S.; Han, M. S.; Mirkin, C. A. "Colorimetric Detection of Mercuric Ion (Hg^{2+}) in Aqueous Media Using DNA-Functionalized Gold Nanoparticles," *Angew. Chem. Int. Ed.* **2007**, *46*, 4093-4096.
14. Lee, J.-S.; Lytton-Jean, A. K. R.; Hurst, S.; Mirkin, C. A. "Silver Nanoparticle Oligonucleotide Conjugates Based on Triple Cyclic Disulfide Moieties," *Nano Lett.* **2007**, *7*, 2112-2115.
15. Lee, J.-S.; Seferos, D. S.; Giljohann, D. A.; Mirkin, C. A. "Synthesis, Thermodynamically Controlled Separation, and Characterization of Polyvalent 2-

- nm Gold Nanoparticle-Oligonucleotide Conjugates,” *J. Am. Chem. Soc.* **2008**, *130*, 5430-5431.
16. Lee, J.-S.; Ulmann, P. A.; Han, M. S.; Mirkin, C. A. “A DNA-Gold Nanoparticle Based Colorimetric Competition Assay for the Detection of Cysteine,” *Nano Lett.* **2008**, *8*, 529-533.
 17. Lettan II, R. B.; Woodward, C. C.; Scheidt, K. A. “Stereoselective Synthesis of Highly Substituted γ -Lactams From Acylsilanes,” *Angew. Chem. Int. Ed.* **2008**, *46*, 7806-7809.
 18. Lytton-Jean, A. K. R.; Han, M. S.; Mirkin, C.A. “Microarray Detection of Duplex and Triplex DNA Binders with DNA-Modified Gold Nanoparticles,” *Analytical Chem.* **2007**, *79*, 6037-6041.
 19. Masar, M. S. III; Gianneschi, N. C.; Oliveri, C. G.; Stern, C. L.; Nguyen, S. T.; Mirkin, C. A. “Allosterically Regulated Supramolecular Catalysis of Acyl Transfer Reactions for Signal Amplification and Detection of Small Molecules,” *J. Am. Chem. Soc.* **2007**, *129*, 10149-10158.
 20. Mattson, A. E.; Scheidt, K. A. “Nucleophilic Acylation of Quinone Methides: An Umpolung Strategy for the Synthesis of α -Aryl Ketones and Benzofurans,” *J. Am. Chem. Soc.* **2007**, *129*, 4508-4509.
 21. Milgram, B. C.; Eskildsen, K.; Richter, S. M.; Scheidt, W. R., **Scheidt, K. A.** Microwave-Assisted Piloty–Robinson Synthesis of 3,4-Disubstitued Pyrroles, *J. Org. Chem.* **2007**, *72*, 3941-3944.
 22. Oliveri, C. G.; Heo, J.; Nguyen, S. T.; Mirkin, C. A.; Wawrzak, Z. “A Convergent Coordination Chemistry-Based Approach to Dissymmetric Macrocyclic Cofacial Porphyrin Complexes,” *Inorganic Chem.* **2007**, *46*, 7716-7718.
 23. Oliveri, C. G.; Nguyen, S.; Mirkin, C. A. “A Highly Modular and Convergent Approach for the Synthesis of Stimulant-Responsive Heteroligated Cofacial Porphyrin Tweezer Complexes,” *Inorg. Chem.* **2008**, *47*, 2755-2763.
 24. Park, S. Y.; Lytton-Jean, A. K. R.; Lee, B.; Weigand, S.; Schatz, G. C.; Mirkin, C. A. “DNA-Programmable Nanoparticle Crystallization,” *Nature* **2008**, *451*, 553-556.
 25. Phillips, E. M.; Reynolds, T. E.; Scheidt, K. A. “Enantioselective Homoenolate Additions to Nitrones Catalyzed by *N*-Heterocyclic Carbenes,” *J. Am. Chem. Soc.* **2008**, *130*, 2416-2417.
 26. Reynolds, T. E.; Scheidt, K. A. “Catalytic Enantioselective α -Acylvinyl Addition Reactions of Silyloxyallenes,” *Angew. Chem Int. Ed.* **2007**, *46*, 7806-7809.
 27. Reynolds, T. E.; Stern, C.; **Scheidt, K. A.** “*N*-Heterocyclic Carbene-Initiated α -Acylvinyl Anion Reactivity: Additions of α -Hydroxy-propargylsilanes to Aldehydes,” *Org. Lett.* **2007**, *9*, 2581-2584.
 28. Scheidt, K. A. and Mattson, A. E. “5-(1,1-dimethylethyl)-5,6-dihydro-2-phenyl-(5*S*)-oxazolo[2,3-*c*]-1,2,4-triazolium tetrafluoroborate.” in *The Electronic Encyclopedia of Reagents for Organic Synthesis*. **2007**.
 29. Stoddart, J. F.; Colquhoun, H. M. “Big and Little Meccano,” *Tetrahedron* **2008**, *64*, 8231–8263.
 30. Ulmann, P. A.; Brown, A. M.; Ovchinnikov, M. V.; Mirkin, C. A.; DiPasquale, A. G.; Rheingold, A. L. “Spontaneous Formation of Heteroligated PtII Complexes

- with Chelating Hemilabile Ligands,” *Chemistry – A European Journal* **2007**, *13*, 4529-4534.
31. Wadamoto, M.; Scheidt, K. A. “Enantioselective Synthesis of α,α -Disubstituted Cyclopentenones by *N*-Heterocyclic Carbene-Catalyzed Desymmetrization of 1,3-Diketones,” *J. Am. Chem. Soc.* **2007**, *129*, 10098-10099.
 32. Xu, X.; Han, M. S.; Mirkin, C. A. “A Gold Nanoparticle-Based, Real-Time Colorimetric Screening Method for Endonuclease Activity and Inhibition,” *Angew. Chem. Int. Ed.* **2007**, *46*, 3468-3470.
 33. Xu, X.; Georganopoulou, D. G.; Hill, H. D.; Mirkin, C. A. “Homogeneous Detection of Nucleic Acids Based upon the Light Scattering Properties of Silver-Coated Nanoparticle Probes,” *Analytical Chem.* **2007**, *79*, 6650-6654.
 34. Xue, C.; Metraux, G. S.; Millstone, J. E.; Mirkin, C. A. “A Mechanistic Study of Photomediated Triangular Silver Nanoprism Growth” *J. Am. Chem. Soc.* **2008**, in press.
 35. Yoon, H. J.; Heo, J.; Mirkin, C. A. “Allosteric Regulation of Phosphate Diester Transesterification Based Upon a Dinuclear Zinc Catalyst Assembled via the Weak-Link Approach,” *J. Am. Chem. Soc.* **2007**, *129*, 14182-14183.
 36. Bae, Y.-S.; Farha, O. K.; Spokoyny, A. M.; Mirkin, C. A.; Hupp, J. T.; Snurr, R. Q. “Carborane-Based Metal-Organic Frameworks as Highly Selective Sorbents for CO₂ Over Methane,” *Chem. Comm.*, **2008**, 4135 - 4137. *Highlighted by "Nature Chemistry"*
 37. Chen, X.; Jeon, Y.-M.; Jang, J.-W.; Qin, L.; Huo, F.; Wei, W.; Mirkin, C. A. “On-Wire Lithography-Based Molecular Transport Junctions: A New Testbed for Molecular Electronics,” *J. Am. Chem. Soc.* **2008**, *130*, 8166-8168.
 38. Chen, X.; Zheng, G.; Cutler, J.; Jang, J.-W.; Mirkin, C. A. “In-Wire Conversion” of a Metal Nanorod Segment into an Organic Semiconductor,” *Small* **2009**, *5*, 1527-1530.
 39. Farha, O.; Spokoyny, A.; Hauser, B.; Bae, Y.-S.; Brown, S.; Snurr, R.; Mirkin, C. A.; Hupp, J. “Synthesis, Properties, and Gas Separation Studies of a Robust Diimide-Based Microporous Organic Polymer,” *Chem. Materials* **2009**, *21*, 3033-3035.
 40. Gadzikwa, T.; Zeng, B.-S.; Hupp, J. T.; Nguyen, S. T. “Ligand Elaboration as a Strategy for Engendering Structural Diversity in Porous Metal-Organic Framework Compounds,” *Chem. Commun.* **2008**, 3672-3674.
 41. Gadzikwa, T.; Mulfort, K. L.; Farha, O. K.; Nguyen, S. T.; Hupp, J. T. “A Zn-Based, Pillared Paddlewheel MOF Containing Free Carboxylic Acids via Covalent Post-Synthesis Elaboration,” *Chem. Comm.*, **2009**, 3720-3722.
 42. Gadzikwa, T.; Lu, G.; Stern, C. L.; Wilson, S. R.; Hupp, J. T.; Nguyen, S. T. “Covalent Surface Modification of a Metal-Organic Framework: Selective Surface Engineering via Cu^I-Catalyzed Huisgen Cycloaddition,” *Chem. Comm.*, **2008**, 43, 5493-5495.
 43. Gadzikwa, T.; Farha, O. K.; Malliakas, C. D.; Kanatzidis, M. G.; Hupp, J. T.; Nguyen, S. T. “Selective Bifunctional Modification of a Non-Catenated Metal-Organic Framework Material via “Click” Chemistry,” *J. Am. Chem. Soc.* **2009**, *131*, 13613-13615.

44. Galliford, C. V. and Scheidt, K. A. "An Unusual Dianion Equivalent from Acylsilanes for the Synthesis of Substituted β -Keto Esters," *Chem. Comm.* **2008**, 1926-1928.
45. Gibbs-Davis, J. M.; Kruk, J. J.; Konek, C. T.; Scheidt, K. A.; Geiger, F. M. "Jammed Acid-Base Reactions at Interfaces," *J. Am. Chem. Soc.* **2008**, *130*, 15444-15447.
46. Hill, H. D.; Hurst, S. J.; Mirkin, C. A. "Curvature-Induced Base Pair "Slipping" Effects in DNA-Nanoparticle Hybridization," *Nano Letters* **2009**, *9*, 317-321.
47. Hurst, S. J.; Hill, H. D.; Mirkin, C. A. "Three-Dimensional Hybridization with Apparently Non-Complementary Polyvalent DNA-Gold Nanoparticle Conjugates," *J. Am. Chem. Soc.* **2008**, *130*, 12192-12200.
48. Jeon, Y.-M.; Kim, D.; Mirkin, C. A.; Golen, J. A.; Rheingold, A. L. "Pyrene-Appended Fluorescent Tweezers Generated via the Weak-Link Approach," *Tetrahedron* **2008**, *64*, 8428-8434.
49. Jeon, Y.-M.; Armatos, G.; Kim, D.; Kanatzidis, M. G.; Mirkin, C. A. "Troeger's Base Derived Infinite Coordination Polymer Microparticles," *Small* **2009**, *5*, 46-50.
50. Lee, J.-S.; Mirkin, C. A. "Chip-Based Scanometric Detection of Mercuric Ion (Hg^{2+}) Using DNA-Functionalized Gold Nanoparticles," *Analytical Chem.* **2008**, *80*, 6805-6808.
51. Lee, S. J.; Hupp, J. T.; Nguyen, S. T. "Growth of Narrowly Dispersed Porphyrin Nanowires and Their Hierarchical Assembly into Macroscopic Columns," *J. Am. Chem. Soc.* **2008**, *130*, 9632-9633.
52. Lee, S. J.; Jensen, R. A.; Malliakas, C. D.; Kanatzidis, M. G.; Hupp, J. T.; Nguyen, S. T. "Effect of Secondary Substituent on the Physical Properties, Crystal Structures, and Nanoparticle Morphologies of (porphyrin) $\text{Sn}(\text{OH})_2$: Diversity Enabled via Synthetic Manipulations," *J. Mater. Chem.* **2008**, *18*, 3640-3642.
53. Lee, S. J.; Malliakas, C. D.; Kanatzidis, M. G.; Hupp, J. T.; Nguyen, S. T. "Amphiphilic Porphyrin Nanocrystals: Morphology Tuning and Hierarchical Assembly," *Adv. Mater.* **2008**, *20*, 3543-3549.
54. Lee, S. J.; Cho, S.-H.; Mulfort, K. L.; Tiede, D. M.; Hupp, J. T.; Nguyen, S. T. "Cavity-Tailored, Self-Sorting Supramolecular Catalytic Boxes for Selective Oxidation," *J. Am. Chem. Soc.*, **2008**, *130*, 16828-16829.
55. Lee, J. Y.; Farha, O. K.; Roberts, J.; Scheidt, K. A.; Nguyen, S. T.; Hupp, J. T. "Metal Organic Framework Materials as Catalysts," *Chem. Soc. Rev.*, **2009**, *38*, 1450-1459.
56. Lee, J. Y.; Roberts, J. M.; Farha, O. K.; Sarjeant, A. A.; Scheidt, K. A.; Hupp, J. T. "Synthesis and Gas Sorption Properties of a Metal-Azolium Framework Material," *Inorg. Chem.*, **2009**, *48*, 9971-9973.
57. Li, Q.; Zhang, W.; Miljanić, Š. O.; Sue, C.-H.; Zhao, Y.-L.; Liu, L.; Knobler, C. B.; Stoddart, J. F.; Yaghi, O. M. "Docking in Metal-Organic Frameworks," *Science* **2009**, *325*, 855-859.
58. Macfarlane, R. J.; Lee, B.; Hill, H. D.; Senesi, A. J.; Seifert, S.; Mirkin, C. A. "DNA-Directed Colloidal Crystal Formation: Assembly and Reorganization," *Proc. Natl. Acad. Sci. USA* **2009**, *106*, 10493-10498.

59. Maki, B. E.; Chan, A.; Scheidt, K. A. "N-Heterocyclic Carbene-Catalyzed Conversion of α,β -Unsaturated Aldehydes to Esters" *Synthesis*, invited Feature Article. **2008**, 1306-1315.
60. Maki, B. E. and Scheidt, K. A. "N-Heterocyclic Carbene-Catalyzed Oxidation of Unactivated Aldehydes to Esters," *Org. Lett.* **2008**, *10*, 4331-4334.
61. Maki, B. E. Phillips, E. M.; Scheidt, K. A. "N-Heterocyclic Carbene-Catalyzed Oxidations" *Tetrahedron*, invited article for special Justin DuBois Issue. **2009**, *65*, 3102-3109.
62. Maki, B. E.; Scheidt, K. A. "Catalytic Dehydrogenative Coupling of Alcohols and Indoles," *Org. Lett.* **2009**, *11*, 1651-1654.
63. Mathies, A. K.; Mattson, A. E.; Scheidt, K. A. "Intermolecular Crossed-Acyloin Reactions by Fluoride-Promoted Additions of *O*-Silyl Thiazolium Carbinols," *Synthesis*, Invited Contribution to Special Edition For Journal Awardees. **2009**, 377-383.
64. Oliveri, C. G.; Ulmann, P. A.; Wiester, M. J.; Mirkin, C. A. "Heteroligated Supramolecular Coordination Complexes Formed via the Halide Induced Ligand Rearrangement Reaction," *Acc. Chem. Res.* **2008**, *41*, 1618-1629.
65. Olson, M. A.; Braunschweig, A. B.; Fang, L.; Ikeda, T.; Klajn, R.; Trabolsi, A.; Mirkin, C. A. Grzybowski, B. A.; Stoddart, J. F. "A Bistable Poly[2]catenane Forms Nanosuperstructures," *Angew. Chem. Int. Ed.* **2009**, *48*, 1792-1797.
66. Phillips, E. M.; Wadamoto, M.; Scheidt, K. A. "N-Heterocyclic Carbene-Catalyzed Desymmetrizations," *Synthesis*, **2009**, 687-690.
67. Phillips, E. M.; Wadamoto, M.; Roth, H. E.; Scheidt, K. A. "N-Heterocyclic Carbene-Catalyzed Michael Reactions of Aryloxyaldehydes," *Org. Lett.* **2009**, *11*, 105-108.
68. Reynolds, T. E.; Binkely, M. S.; Scheidt, K. A. "Lewis Acid-Catalyzed Conjugate Additions of Silyloxyallenes: A Selective Solution to the Intermolecular Rauhut-Currier Problem," *Org. Lett.* **2008**, *10*, 2449-2452.
69. Reynolds, T. E.; Binkely, M. S.; Scheidt, K. A. "Highly Selective α -Acylvinyl Anion Additions to Imines," *Org. Lett.* **2009**, *10*, 5227-5230.
70. Shultz, A. M.; Farha, O. K.; Hupp, J. T.; Nguyen, S. T. "A Catalytically Active, Permanently Microporous MOF with Metalloporphyrin Struts," *J. Am. Chem. Soc.*, **2009**, *131*, 4204-4205.
71. Spokoyny, A. M.; Kim, D.; Sumrein, A.; Mirkin, C. A. "Infinite Coordination Polymer Nano- and Microparticle Structures," *Chem. Soc. Rev.* **2009**, *38*, 1218-1227.
72. Stokes, G. Y.; Buchbinder, A. M.; Gibbs-Davis, J. M.; Scheidt, K. A.; Geiger, F. M. "Heterogeneous Ozone Oxidation Reactions of 1-Pentene, Cyclopentene, Cyclohexene, and a Menthenol Derivative Studied by Sum Frequency Generation," *J. Phys. Chem. A*. **2008**, *112*, 11688-11698.
73. Tsonchev, S.; Niece, K. L.; Schatz, G. C.; Ratner, M. A.; Stupp, S. I. "Phase Diagram for Assembly of Biologically-Active Peptide Amphiphiles," *J. Phys. Chem. B* **2008**, *112*, 441-447.
74. Xu, L.; Ding, Y.; Catalona, W. J.; Yang, X.; Anderson, W. F.; Jovanovic, B.; Wellman, K.; Kilmer, J.; Huang, X.; Scheidt, K. A.; Montgomery, R. B.; Bergan,

- R. C. "MEK4 Function, Genistein Treatment, and Invasion of Human Prostate Cancer Cells," *J. Nat. Can. Inst.* **2009**, *101*, 1141 – 1155.
75. Yoo, H.; Mirkin, C. A.; DiPasquale, A. G.; Rheingold, A. L.; Stern, C. L. "Reversible CO-Induced Chloride Shuttling in Rh(I) Tweezer Complexes Containing Urea Functionalized Hemilabile Ligands," *Inorg. Chem.* **2008**, *47*, 9727-9729.
 76. Youm, K.-T.; Nguyen, S. T.; Hupp, J. T. "Hollow Porphyrin Prisms: Modular Formation of Permanent, Torsionally Rigid, Nanostructures via Templated Olefin Metathesis," *Chem. Comm.*, **2008**, 29, 3375-3377.
 77. Yoon, H. J.; Mirkin, C. A. "PCR-Like Cascade Reactions in the Context of an Allosteric Enzyme Mimic," *J. Am. Chem. Soc.* **2008**, *130*, 11590-11591.
 78. Zheng, G.; Daniel, W. L.; Mirkin, C. A. "A New Approach to Amplified Telomerase Detection with Polyvalent Oligonucleotide Nanoparticle Conjugates," *J. Am. Chem. Soc.* **2008**, *130*, 9644-9645
 79. Zheng, G. F.; Chen, X. D.; Mirkin, C. A. "Complementary Electrical and Spectroscopic Detection Assays with On-Wire-Lithography-Based Nanostructures," *Small* **2009**, *5*, 2537-2540.
 80. Zheng, G.; Qin, L.; Mirkin, C. A. "Spectroscopically Enhancing Electrical Nanotrap," *Angew. Chem. Int. Ed.* **2008**, *47*, 1938-1941.
 81. O. K. Farha, A. Ö. Yazaydin, I. Eryazici, C. D. Malliakas, B. G. Hauser, M. G. Kanatzidis, S. T. Nguyen, R. Q. Snurr, J. T. Hupp, "De Novo Synthesis of a Metal-Organic Framework Material Featuring Ultra-High Surface Area and Extraordinary Gas Storage Capacities" *Nature Chem.*, **2010**, *2*, 944-948.
 82. O. K. Farha, A. M. Shultz, A. A. Sarjeant, S. T. Nguyen, J. T. Hupp, "Active-Site-Accessible, Porphyrinic Metal-Organic Framework Materials," *J. Am. Chem. Soc.*, **2011**, *133*, 5652–5655.
 83. "Metal-Organic Frameworks as Sensors: A ZIF-8 Based Fabry-Pérot Device as A Selective Sensor for Chemical Vapors and Gases," G. Lu, J. T. Hupp, *J. Am. Chem. Soc.*, **2010**, *132*, 7832–7833.
 84. O. K. Farha, Y. Bae, B. G. Hauser, A. M. Spokoyny, R. Q. Snurr, C. A. Mirkin and J. T. Hupp, "Chemical Reduction of a Diimide based Porous Polymer for Selective Uptake of Carbon Dioxide versus Methane," *Chem. Commun.*, **2010**, 1056-1058.
 85. Y. Bae, A. M. Spokoyny, O. K. Farha, R. Q. Snurr, J. T. Hupp, C. A. Mirkin, "Separation of Gas Mixtures Using Co(II)-Carborane-Based Porous Coordination Polymers," *Chem. Commun.*, **2010**, 3478-3480.
 86. "Gas Sorption Properties of Cobalt(II) Carborane-Based Coordination Polymers As a Function of Morphology" O. K. Farha, A. M. Spokoyny, K. L. Mulfort, S. Galli, J. T. Hupp, C. A. Mirkin, *Small*, **2009**, *5*, 1727-1731.
 87. Li, Q.; Zhang, W.; Miljanić, Š. O.; Knobler, C. B.; Stoddart, J. F.; Yaghi, O. M. "A Metal-Organic Framework Replete with Ordered Donor–Acceptor Catenanes," *Chem. Commun.* **2010**, 46, 380–382.
 88. Spokoyny, A.; Rosen, M. S.; Ulmann, P. A.; Stern, C.; Mirkin, C. A. "Selective Formation of Heteroligated Pt(II) Complexes with Bidentate Phosphine-Thioether (P, S) and Phosphine-Selenoether (P, Se) Ligands via the Halide-Induced Ligand Rearrangement Reaction", *Inorganic Chemistry*, **2009**, *49*, 1577-1586.

89. Xu, X.; Daniel, W. L.; Wei, W.; Mirkin, C. A. "Colorimetric Cu²⁺ Detection Using DNA Modified Gold Nanoparticle Aggregates as Probes and Click Chemistry," *Small* **2010**, 6, 623-626.
90. Wiester, M. J.; Mirkin, C. A. "Water-Soluble Macrocycles Synthesized via the Weak-Link Approach," *Inorg. Chem.* **2009**, 48, 8054-8056.
91. Kuwabara, J.; Yoon, H. J.; Mirkin, C. A.; DiPasquale, A. G.; Rheingold, A. L. "Pseudo-Allosteric Regulation of the Anion Binding Affinity of a Macrocyclic Coordination Complex," *Chem. Comm.* **2009**, 4557-4559.
92. Spokoyny, A. M.; Reuter, M. G.; Stern, C. L.; Ratner, M. A.; Seideman, T.; Mirkin, C. A. "Carborane-Based Pincers: Synthesis and Structure of SeBSe and SBS Pd(II) Complexes," *J. Am. Chem. Soc.* **2009**, 131, 9482-9483.
93. Daniel, W. L.; Han, M. S.; Lee, J.-S.; Mirkin, C. A. "Colorimetric Nitrite and Nitrate Detection with Gold Nanoparticle Probes and Kinetic Endpoints," *J. Am. Chem. Soc.* **2009**, 131, 6362-6363.
94. Ulmann, P. A.; Braunschweig, A. B.; Lee, O.-S.; Wiester, M.; Schatz, G. C.; Mirkin, C. A. "Inversion of Product Selectivity in an Enzyme-Inspired Metallosupramolecular Tweezer Catalyzed Epoxidation Reaction," *Chem. Comm.* **2009**, 5121-5123.
95. Ulmann, P. A.; Mirkin, C. A.; DiPasquale, A. G.; Liable-Sands, L. M.; Rheingold, A. L. "Reversible Ligand Pairing and Sorting Processes Leading to Heteroligated Palladium(II) Complexes with Hemilabile Ligands," *Organometallics* **2009**, 28, 1068-1074.
96. Wiester, M. J.; Ulmann, P. A.; Mirkin, C. A. "Enzyme Mimics Based Upon Supramolecular Coordination Chemistry," *Angew. Chem.*, **2011**, 50, 114-137.
97. Spokoyny, A. M.; Li, T.; Farha, O. K.; Machan, C. W.; She, C.; Stern, C. L.; Marks, T. J.; Hupp, J. T.; and Mirkin, C. A. "Electronic Tuning of Ni-based Bis(dicarbollide) Redox Shuttles In Dye-Sensitized Solar Cells," *Angew. Chem.*, **2010**, 49, 5339-5343.
98. Spokoyny, A. M.; Farha, O. K.; Mulfort, K. L.; Hupp, J. T.; Mirkin, C. A. "Porosity Tuning of Carborane-Based Metal Organic Frameworks (MOFs) via Coordination Chemistry and Ligand Design," *Inorg. Chim. Acta*, **2010**, 364, 266-271.
99. Wiester, M.; Braunschweig, A. B.; Mirkin, C. A. "Solvent and Temperature Induced Switching Between Structural Isomers of RhI Phosphinoalkyl Thioether (PS) Complexes," *Inorganic Chemistry*, **2010**, 49, 7188-7196.
100. Yoon, H. J.; Kuwabara, J.; Kim, J.-H.; Mirkin, C. A. "Allosteric Supramolecular Triple-Layer Catalysts," *Science*, **2010**, 330, 66-69.
101. Li, T. C.; Fabregat-Santiago, F.; Farha, O. K.; Spokoyny, A. M.; Ruiz, S.; Bisquert, J.; Mirkin, C. A.; Marks, T. J.; Hupp, J. T. "SiO₂ Aerogel-templated, Porous TiO₂ Photoanodes for Enhanced Performances in Dye-Sensitized Solar Cells Containing a Ni(III)/(IV) Bis(dicarbollide) Shuttle," *J. Phys. Chem. C.*, **2011**, 115, 11257-11264.
102. Machan, C. W.; Spokoyny, A. M.; Jones, M. R.; Sarjeant, A. A.; Stern, C. L.; Mirkin, C. A. "The Plasticity of the Nickel(II) Coordination Environment in Complexes with Hemilabile Phosphino-Thioether Ligands," *J. Am. Chem. Soc.*, **2011**, 133, 3023-3033.

103. Rosen, M. S.; Spokoyny, A. M.; Machan, C. W.; Stern, C. L.; Sarjeant, A. A.; Mirkin, C. A. "Chelating Effect as a Driving Force for the Selective Formation of Heteroligated Pt(II) Complexes with Bidentate Phosphino-Chalcoether Ligands," *Inorganic Chemistry*, **2011**, *50*, 1411–1419.
104. Shultz, A. M.; Farha, O. K.; Adhikari, D.; Sarjeant, A. A.; Hupp, J. T.; Nguyen, S. T. "Selective surface and near-surface modification of a non-catenated, catalytically active metal-organic framework material based on Mn(salen) struts," *Inorg. Chem.* **2011**, *50*, 1700-1703. DOI: 10.1021/ic101952y.
105. Schultz, A. M.; Farha, O. K.; Hupp, J. T.; Nguyen, S. T. "Synthesis of catalytically active porous organic polymers from metalloporphyrin building blocks," *Chem. Sci.* **2011**, *2*, 686-689.
106. Lee, C. Y.; Bae, Y.-S.; Jeong, N. C.; Farha, O. K.; Sarjeant, A. A.; Stern, C. L.; Nickias, P.; Snurr, R. Q.; Hupp, J. T.; Nguyen, S. T.; Snurr, R. Q. "Kinetic Separation of Propene and Propane in Metal-Organic Frameworks: Controlling Diffusion Rates in Plate-Shaped Crystals via Tuning of Pore Apertures and Crystallite Aspect Ratios" *J. Am. Chem. Soc.*, **2011**, *133*, 5228-5231.
107. Schultz, A. M.; Sarjeant, A. A.; Farha, O. K.; Hupp, J. T.; Nguyen, S. T. "Post-synthesis modification of a metal-organic framework to form metallosalen-containing MOF materials," *J. Am. Chem. Soc.*, **2011**, *133*, 13252–13255.
108. "Two Azolium Rings are Better than One: A Strategy for Modulating Catenation and Pore Size in Cu and Zn Metal-Organic Frameworks," J. Roberts, O. K. Farha, J. T. Hupp, K. A. Scheidt, *Cryst. Growth Des.* **2011**, *11*, 4747–4750.
109. Ibrahim Eryazici[‡], Omar K. Farha[‡], Owen C. Compton, Charlotte Stern, Joseph T. Hupp and SonBinh T. Nguyen, "Luminescent infinite coordination polymer materials from metal-terpyridine ligation" *Dalton Trans.*, 2011, **40**, 9189-9193.
110. "Rational Design, Synthesis, Purification and Activation of Metal-Organic Framework Materials," O. K. Farha and J. T. Hupp, *Acc. Chem. Res.*, **2010**, *43*, 1166–1175.
111. "Cubic and rhombohedral heterobimetallic networks constructed from uranium, transition metals, and phosphonoacetate: new methods for constructing porous materials," A. N. Alsobrook, B. G. Hauser, J. T. Hupp, E. V. Alekseev, W. Depmeier, T. E. Albrecht-Schmitt, *Chem. Commun.* **2010**, *46*, 9167-9169.
112. Spruell, J. M.; Coskun, A.; Friedman, D. C.; Forgan, R. S.; Sarjeant, A. A.; Trabolsi, A.; Fahrenbach, A. C.; Barin, G.; Paxton, W. F.; Dey, S. K.; Olson, M. A.; Benítez, D.; Tkatchouk, E.; Colvin, M. T.; Carmielli, R.; Caldwell, S. T.; Rosair, G. M.; Hewage, S. G.; Duclairoir, F.; Seymour, J. L.; Slawin, A. M. Z.; Goddard III, W. A.; Wasielewski, M. R.; Cooke, G.; Stoddart, J. F. "Highly stable TTF radical dimers in [3]catenanes," *Nature Chem.* **2010**, *2*, 870–879.
113. Wang, C.; Olson, M. A.; Fang, L.; Benitez, D.; Tkatchouk, E.; Basu, S.; Basuray, A. N.; Zhang, D. Q.; Zhu, D. B.; Goddard, W. A.; Stoddart, J. F. "Isolation by crystallization of translational isomers of a bistable donor-acceptor [2]catenane," *Proc. Natl. Acad. Sci. USA* **2010**, *107*, 13991–13996.
114. Gasa, T. B.; Valente, C.; Stoddart, J. F. "Solution-phase counterion effects in supramolecular and mechanostereochemical systems," *Chem. Soc. Rev.* **2011**, *40*, 57–78.

115. Fang, L.; Basu, S.; Sue, C. H.; Fahrenbach, A. C.; Stoddart, J. F. "Syntheses and dynamics of donor-acceptor [2]catenanes in water," *J. Am. Chem. Soc.* **2011**, *133*, 396–399.
116. "Metal-Adeninate Vertices for the Construction of an Exceptionally Porous Metal-Organic Framework," J. An, O. K. Farha, J. T. Hupp, E. Pohl, J. Yeh, and N. L. Rosi, *Nature Comm.* **2012**, *3*, 604.
117. Fang, L.; Wang, C.; Fahrenbach, A. C.; Trabolsi, A.; Botros, Y. Y.; Stoddart, J. F. "Dual stimulus switching of a [2]catenane in water," *Angew. Chem. Int. Ed.* **2011**, *50*, 1805–1809.
118. "Light-Harvesting Metal-Organic Frameworks (MOFs): Efficient Strut-to-Strut Energy Transfer in Bodipy and Porphyrin-based MOFs," C. Y. Lee, O. K. Farha, B. J. Hong, A. A. Sarjeant, S. T. Nguyen, J. T. Hupp, *J. Am. Chem. Soc.* **2011**, *133*, 15858–15861.
119. Gassensmith, J. J.; Erne, P. M.; Paxton, W. F.; Valente, C.; Stoddart, J. F. "Microcontact click printing for templating ultrathin films of metal-organic frameworks," *Langmuir* **2011**, *27*, 1341–1345.
120. Coskun, A.; Spruell, J. M.; Barin, G.; Fahrenbach, A. C.; Forgan, R. S.; Colvin, M. T.; Carmielli, R.; Benítez, D.; Tkatchouk, E.; Friedman, D. C.; Sarjeant, A. A.; Wasielewski, M. R.; Goddard III, W. A.; Stoddart, J. F. "Mechanically stabilized tetrathiafulvalene radical dimers," *J. Am. Chem. Soc.* **2011**, *133*, 4538–4547.
121. Stoll, R. S.; Friedman, D. C.; Stoddart, J. F. "Mechanically interlocked mechanophores by living-radical polymerization from rotaxane initiators," *Org. Lett.* **2011**, *13*, 2706–2709.
122. "High Propene/Propane Selectivity in Isostructural Metal-Organic Frameworks with High Densities of Open Metal Sites" Bae, Y.-S.; Lee, C. Y.; Kim, K. C.; Farha, O. K.; Nickias, P.; Hupp, J. T.; Nguyen, S. T.; Snurr, R. Q. *Angew. Chem. Int. Ed.* **2011**, *51*, 1857–1860.
123. Spokoyny, A. M.; Machan, C. W.; Clingerman, D. J.; Rosen, M. S.; Wiester, M. J.; Kennedy, R. D.; Stern, C. L.; Sarjeant, A. A.; Mirkin, C. A. "A Coordination Chemistry Dichotomy for Icosahedral Carborane-Based Ligands," *Nature Chem.*, **2011**, *3*, 590–596.
124. Trabolsi, A.; Khashab, N.; Fahrenbach, A. C.; Friedman, D. C.; Colvin, M. T.; Cotí, K. K.; Benítez, D.; Tkatchouk, E.; Olsen, J.-C.; Belowich, M. E.; Carmielli, R.; Khatib, H. A.; Goddard III, W. A.; Wasielewski, M. R.; Stoddart, J. F. "Radically enhanced molecular recognition," *Nature Chem.* **2010**, *2*, 42–49.
125. Fang, L.; Olson, M. A.; Stoddart, J. F. "Mechanically bonded macromolecules," *Chem. Soc. Rev.* **2010**, *39*, 17–29.
126. Trabolsi, T.; Fahrenbach, A. C.; Share, A. I.; Friedman, D. C.; Gasa, T. B.; Dey, S. K.; Khashab, N. M.; Saha, S.; Aprahamian, I.; Khatib, H. A.; Flood, A. H.; Stoddart J. F. "A tristable [2]pseudo[2]rotaxane" *Chem. Commun.* **2010**, *46*, 871–873.
127. Yasuda, T.; Tanabe, K.; Tsuji, T.; Cotí, K. K.; Aprahamian, I.; Stoddart, J. F.; Kato, T. "A redox-switchable [2]rotaxane in a liquid-crystalline state" *Chem. Commun.* **2010**, *46*, 1224–1226.

128. Deng, H.; Olson, M. A.; Stoddart, J. F.; Yaghi, O. M. "Robust dynamics," *Nature Chem.* **2010**, *2*, 439–443.
129. Li, H.; Fahrenbach, A. C.; Coskun, A.; Zhu, Z.; Barin, G.; Zhao, Y.-L.; Botros, Y. Y.; Sauvage, J.-P.; Stoddart, J. F. "A light-stimulated molecular machine driven by radical pairing interactions in water," *Angew. Chem. Int. Ed.* **2011**, *50*, 6782–6788.
130. Olsen, J.-C.; Fahrenbach, A. C.; Trabolsi, A.; Friedman, D.C.; Dey, S. K.; Gothard, C. M.; Shveyd, A. K.; Gasa, T. B.; Spruell, J. M.; Olson, M. A.; Wang, C.; Jacquot de Rouville, H.-P.; Botros, Y. Y.; Stoddart, J. F. "A neutral redox-switchable [2]rotaxane," *Org. Biomol. Chem.* **2011**, *9*, 7126–7133.
131. "Imparting Functionality to a Metal-Organic Framework Material by Controlled Encapsulation of Nanoparticles," G. Lu, S. Li, Z. Guo, B. G. Hauser, O. K. Farha, X. Qi, Y. Wang, X. Wang, X. Liu, H. Zhang, Q. Zhang, X. Chen, J. Ma, L. Joachim, Y. Yang, J. T. Hupp and F. Huo, *Nature Chem.* **2012**, *4*, 310–316.
132. "Synthesis and Metallation of Catechol-functionalized Porous Organic Polymers," M. H. Weston, O. K. Farha, B. G. Hauser, J. T. Hupp, and S. T. Nguyen, *J. Chem. Mater.*, **2012**, *24*, 1292–1296.
133. "Catalytically Active Supramolecular Porphyrin Boxes: Acceleration of the Methanolysis of Phosphate Triesters via a Combination of Increased Local Nucleophilicity and Reactant Encapsulation," B. Kang, J. W. Kurutz, K-T. Youm, R. K. Totten, J. T. Hupp, and S. T. Nguyen, *Chem. Sci.*, **2012**, *3*, 1938–1944.
134. "Fabrication of Metal-Organic-Framework-containing Silica-Colloidal Crystals for Vapor Sensing," G. Lu, O. K. Farha, L. E. Kreno, P. M. Schoenecker, K. S. Walton, R. P. Van Duyne, and J. T. Hupp, *Adv. Mater.* **2011**, *23*, 4449–4452.
135. Machan, C. W.; Lifschitz, A. M.; Stern, C. L.; Sarjeant, A. A.; Mirkin, C. A. "Crystallographic Snapshots of the Bond-breaking Isomerization Reactions Involving Ni(II) Complexes with Hemilabile Ligands," *Angew. Chem. Int. Ed.*, **2011**, *124*, 1498–1501.
136. Pandey, P.; Farha, O. K.; Spokoyny, A. M.; Thomes, M.; Mirkin, C. A.; Kanatzidis, M. G.; Hupp, J. T.; Nguyen, S. T. "Click-Based" Porous Organic Polymers From Tetrahedral Building Blocks" *J. Mater. Chem.* **2011**, *21*, 1700–1703.
137. Fahrenbach, A. C.; Barnes, J. C.; Lanfranchi, D. A.; Li, H.; Coskun, A.; Gassensmith, J. J.; Liu, Z.; Benítez, D.; Trabolsi, A.; Goddard III, W. A.; Elhabiri, M.; Stoddart, J. F. "Solution-phase mechanistic study and solid-state structure of a tris(bipyridinium radical cation) inclusion complex," *J. Am. Chem. Soc.* **2012**, *134*, 3061–3072.
138. Belowich, M. E.; Stoddart, J. F.; "Dynamic imine chemistry," *Chem. Soc. Rev.* **2012**, *41*, 2003–2024.
139. Belowich, M. E.; Valente, C.; Smaldone, R. A.; Friedman, D. C.; Thiel, J.; Cronin, L.; Stoddart, J. F. "Positive cooperativity in the template-directed synthesis of monodisperse macromolecules," *J. Am. Chem. Soc.* **2012**, *134*, 5243–5261.
140. "Enhanced Catalytic Decomposition of a Phosphate Triester by Modularly Accessible Bimetallic Porphyrin Dyads and Dimers," R. K. Totten, P. Ryan, B.

- Kang, S. J. Lee, L. J. Broadbelt, R. Q. Snurr, J. T. Hupp, S. T. Nguyen, *Chem. Commun.* **2012**, 48, 4178-4180.
141. Coskun, A.; Spruell, J. M.; Barin, G.; Dichtel, W. R.; Flood, A. H.; Botros, Y. Y.; Stoddart, J. F. "High hopes: Can molecular electronics realise its potential?" *Chem. Soc. Rev.* **2012**, 41, 4827-4859.
 142. Fahrenbach, A. C.; Bruns, C. J.; Cao, D.; Stoddart, J. F. "Ground-state thermodynamics of bistable redox-active donor-acceptor mechanically interlocked molecules," *Acc. Chem. Res.* In press DOI: 10.1021/ar3000629.
 143. Basuray, A. N.; Jacquot de Rouville, H.-P.; Fahrenbach, A. C.; Ambrogio, M. W.; Avestro, A.-J.; Strutt, N. L.; Hartlieb, K. J.; Bruns, C. J.; Stoddart, J. F. "The chameleonic nature of diazoperopyrenium recognition," *Angew. Chem. Int. Ed.* In press.
 144. Fahrenbach, A. C.; Zhu, Z.; Cao, D.; Liu W.-G.; Li, H.; Dey, S. K.; Basu, S.; Trabolsi, A.; Botros, Y. Y.; Goddard III, W. A.; Stoddart, J. F. "Radically enhanced molecular switches," *J. Am. Chem. Soc.* In press.
 145. Avestro, A.-J.; Belowich, M. E.; Stoddart, J. F. "Cooperative self-assembly: producing synthetic polymers with precise and concise primary structures," *Chem. Soc. Rev.* In press.
 146. Fahrenbach, A. C.; Sampath, S.; Latte, D. J.; Kleinman, S. L.; Valley, N.; Barnes, J. C.; Hartlieb, K. J.; Liu, Z.; Dravid, V. P.; Schatz, G. C.; van Duyne, R. P.; Stoddart, J. F. "A semiconducting organic radical cationic host-guest complex," *ACS Nano* Submitted.
 147. Wang, C.; Dyer, S. M.; Cao, D.; Fahrenbach, A. C.; Horwitz, N.; Colvin, M. T.; Carmieli, R.; Stern, C. L.; Dey, S. K.; Wasielewski, M. R.; Stoddart, J. F. "The role of tetrathiafulvalene heteroradical cation dimerization in a redox-active [2]catenane," *J. Am. Chem. Soc.* Submitted.
 148. "Urea Metal-Organic Frameworks as Effective and Size Selective Hydrogen-Bond Catalysts," J. M. Roberts, B. M. Fini, O. K. Farha, A. A. Sarjeant, J. T. Hupp, and K. A. Scheidt, *J. Am. Chem. Soc.* **2012**, 134, 3334-3337.
 149. "Metal-organic Framework Materials with Ultrahigh Surface Areas: Is the Sky the Limit?" O. K. Farha, I. Eryazici, N. C. Jeong, B. G. Hauser, A. A. Sarjeant, S. T. Nguyen A. Ö. Yazaydin, J. T. Hupp *J. Am. Chem. Soc.*, **2012**, 134, 15016-15021.
 150. "Two Large-Pore Metal-Organic Frameworks Derived from a Single Polytopic Strut," I. Eryazici, O. K. Farha, B. G. Hauser, A. Ö. Yazaydin, A. A. Sarjeant, S. T. Nguyen, and J. T. Hupp *Cryst. Growth Des.* **2012**, 1075-1080.
 151. "N-Heterocyclic Carbene-Like Catalysis by a Metal-Organic Framework (MOF) Material," M. B. Lalonde, O. K. Farha, K. A. Scheidt, J. T. Hupp, *ACS Catalysis*, **2012**, 2, 1550-1554.
 152. "Cyclic Metalloporphyrin Dimers and Tetramers: Tunable Shape-selective Hosts for Fullerenes," B. Kang, R. K. Totten, M. H. Weston, J. T. Hupp, and S. T. Nguyen *Dalton Trans.* **2012**, 41, 12156-12162.
 153. "Solvent-Assisted Linker Exchange (SALE) and Post-Assembly Metallation In Porphyrinic Metal-Organic Framework Materials," S. Takaishi, E. J. DeMarco, M. J. Pellin, O. K. Farha, J. T. Hupp *Chemical Science* **2012**, submitted.
 154. "Opening Up ZIF-8: A Catalytically Active Zeolitic Imidazolate Framework of Sodalite Topology with Unsubstituted Linkers," O. Karagiari, M. Lalonde, W.

- Bury, A. A. Sarjeant, O. K. Farha, J. T. Hupp *J. Am. Chem. Soc.* **2012**, submitted.
155. “Gram-scale, High-yield Synthesis of a Robust Metal–Organic Framework for Storing Methane and Other Gases,” C. E. Wilmer, O. K. Farha, T. Yildirim, I. Eryazici, V. Krungleviciute, A. A. Sarjeant, R. Q. Snurr, J. T. Hupp *Energy Env. Sci.* **2012**, submitted.
156. Machan, C. W.; Adelhardt, M.; Sarjeant, A. A.; Stern, C. L.; Sutter, J.; Meyer, K.; Mirkin, C. A. “‘One-Pot’ Synthesis of an Fe(II) Bis-Terpyridine Complex with Allosterially Regulated Electronic Properties,” *J. Am. Chem. Soc.*, **2012**, in press.
157. Yoo, H.; Rosen, M. S.; Brown, A. M.; Wiester, M. J.; Stern, C. L.; Mirkin, C. A. “Elucidating the Mechanism of the Halide-Induced Ligand Rearrangement Reaction,” *J. Am. Chem. Soc.*, **2012**, submitted.
158. Roy, S.; George, C. B.; Ratner, M. A. “Catalysis by a Zinc-porphyrin based Metal-Organic Framework: From Theory to Computational Design”, *J. Phys. Chem. C* **2012**, submitted.
159. Heitzer, H.; George, C. B.; Ratner, M. A. “Monte-Carlo Analysis of Solvent Effects in Catalytically Active Metal-Organic Frameworks”, in preparation.